Research Square

Preprints are preliminary reports that have not undergone peer review.
They should not be considered conclusive, used to inform clinical practice,
or referenced by the media as validated information.

m¹A on chromatin-associated RNA licenses Pol II pause release and is pharmacologically targetable in glioblastoma

Jeremy Rich

drjeremyrich@gmail.com

UNC Lineberger Comprehensive Cancer Center https://orcid.org/0000-0001-7845-5302

Donghai Wang

University of Pittsburgh

Xujia Wu

Guangdong Provincial People's Hospital https://orcid.org/0000-0002-6904-0778

Chenxi Sun

The University of Chicago

Weichi Wu

University of Pittsburgh

Suchet Taori

University of Pittsburgh

Zhongyu Zou

The University of Chicago

Qiulian Wu

UNC Chapel Hill US

Tengfei Huang

University of Pittsburgh

Daqi Li

Lineberger Comprehensive Cancer Center https://orcid.org/0000-0002-7448-7435

Po Zhang

University of Pittsburgh

Fanen Yuan

University of Pittsburgh

Rui Wang

Hillman Cancer Center, UPMC, University of Pittsburgh

Huan Li

Hillman Cancer Center, UPMC, University of Pittsburgh

Zhiye Chen

UNC Lineberger Comprehensive Cancer Center
Hailong Mi
University of Pittsburgh
Tingting Duan
University of Pittsburgh https://orcid.org/0000-0002-4482-5587
Xiuli Mao
University of Illinois Urbana-Champaign
Huairui Yuan
University of Pittsburgh
Junran Zhang
The James Comprehensive Cancer Center, The Ohio State University
Ya-Ming Hou
ya-ming.hou@jefferson.edu https://orcid.org/0000-0001-6546-2597
Chuan He
The University of Chicago https://orcid.org/0000-0003-4319-7424

Article

Keywords:

Posted Date: November 26th, 2026

DOI: https://doi.org/10.21203/rs.3.rs-11652031/v1

License: This work is licensed under a Creative Commons Attribution 4.0 International License.
Read Full License

Additional Declarations: There is **NO** Competing Interest.

---

m^1A on chromatin-associated RNA licenses Pol II pause release and is pharmacologically targetable in glioblastoma

Donghai Wang[1, 2, 3], Xujia Wu[2, 3], Chenxi Sun[4], Weichi Wu[1, 2, 3], Suchet Taori[2, 3], Zhongyu Zou[4], Qiulian Wu[1, 2, 3], Tengfei Huang[1, 2, 3], Daqi Li[1, 2, 3], Po Zhang[2, 3], Fanen Yuan[2, 3], Rui Wang[1, 2, 3], Huan Li[1, 2, 3], Zhiye Chen[1, 2, 3], Hailong Mi[2, 3], Tingting Duan[2, 3], Xiuli Mao[5], Huairui Yuan[2, 3], Junran Zhang[6], Ya-Ming Hou[7], Chuan He[4], Jeremy N. Rich[1, 2, 8, 9, 10, *]

1. Lineberger Comprehensive Cancer Center, University of North Carolina, Chapel Hill, NC, USA

2. UPMC Hillman Cancer Center, Pittsburgh, PA, USA

3. Department of Medicine, University of Pittsburgh, Pittsburgh, PA, USA

4. Department of Chemistry, The University of Chicago, Chicago, IL, USA

5. School of Chemical Sciences, University of Illinois Urbana-Champaign, Urbana, IL, USA

6. Department of Radiation Oncology, The Ohio State University Comprehensive Cancer Center and College of Medicine, Columbus, OH, USA

7. Department of Biochemistry and Molecular Biology, Thomas Jefferson University, Philadelphia, PA, USA

8. Department of Neurology, University of North Carolina, Chapel Hill, NC, USA

9. Department of Neurology, University of Pittsburgh, Pittsburgh, PA, USA

10. Lead contact

* Correspondence: J.N.R. (drjeremyrich@gmail.com)

Key words: N^1-methyladenosine; chromatin-associated RNA; glioblastoma stem cell; transcription elongation; glioblastoma

ABSTRACT

RNA modifications are post-transcriptional regulators, and whether they instruct transcription itself remains unresolved. Here, we show that N^1-methyladenosine (m^1A) on nascent chromatin-associated RNA (caRNA) induces RNA polymerase II pause release in glioblastoma (GBM). Profiling 55 modifications identified m^1A as selectively enriched in the caRNA of GBM stem cells (GSCs). The SOX2-driven methyltransferase complex, TRMT6/TRMT61A, occupies active promoters and methylates nascent transcripts in oncogenic and glycolytic genes. Writer loss trapped Pol II at promoters and reduced Ser2 phosphorylation across the gene bodies. m^1A-marked caRNA recruited the elongation helicase SETX, and dCas13-directed demethylation of the MYC promoter-proximal caRNA stalled Pol II and collapsed MYC output. TRMT6/TRMT61A loss impaired glycolysis, GSC self-renewal, and tumor propagation. Structure-guided screening identified the brain-penetrant antipsychotic paliperidone as a TRMT61A binder that depletes caRNA m^1A and combines it with ERBB inhibition in orthotopic xenografts. Thus, nascent-RNA methylation constitutes a transcriptional checkpoint and is druggable in GBM.

INTRODUCTION

Tumors comprise diverse and dynamically evolving populations of neoplastic cells with distinct molecular and functional states[1]. Within this heterogeneous compartment, stem-like tumor cells contribute to tumor maintenance, adaptation, and therapeutic resistance, highlighting molecular determinants of cellular plasticity and stemness as promising opportunities for innovative cancer therapeutics[2,3]. GBM stem cells (GSCs) contribute to tumor malignancy through sustained tumor growth and invasion of the normal brain to prevent curative surgical resection, neoangiogenesis, and therapeutic resistance[1,4-6]. Cancer stem cells often display relatively open and active chromatin states that permit dynamic transcriptional control and cell state plasticity that promotes tumor adaption to inhospitable tumor microenvironments and therapeutic insults to drive adaptive resistance[7,8]. GSCs are maintained in a relatively undifferentiated state through the action of core stem cell transcription factors and regulatory circuits[9].

RNA modifications have emerged as a particularly attractive therapeutic opportunity because they couple dynamic control of the cell state with enzymatic activities that are potentially amenable to pharmacological targeting. RNA modifications represent an evolutionarily conserved dimension of gene regulation that dynamically shapes the flow of genetic information from DNA to proteins, orchestrating gene expression programs across all living systems[10-12]. These modifications are precisely controlled during development and cell fate commitment, and aberrant regulation has been increasingly implicated in human diseases, particularly cancer[13-16]. m6A (N6-methyladenosine) is the most common internal modification on mRNA and other types of RNA, regulating mRNA stability, translation, and decay[17-19]. Regulators of m6A (writers, erasers, and readers) have been defined and novel therapeutics have been developed to target their function and inhibit tumor cell growth in several cancer types, including GBM[20-22]. We and others have described the roles of other RNA modifications, including N4-acetylcytidine (ac4C), alternative polyadenylation (APA), RNA editing, 5-methylcytosine (m5C), and pseudouridine (Ψ), in GBM[23-28]. Based on this background, we hypothesized that RNA modifications represent a fertile opportunity to link RNA and tumor biology to discover novel cancer therapeutics.

While most studies on RNA modifications have focused on cytoplasmic RNAs, RNA modifications also decorate nuclear chromatin-associated RNAs (caRNAs), expanding the regulatory network that connects RNA modifications to gene regulation[29-31]. Chromatin-associated RNAs are nascent transcripts that form secondary structures by interacting with the template strand of open chromatin during transcription. This class of regulatory non-coding RNAs encompasses promoter-associated RNAs (paRNAs), enhancer RNAs (eRNAs), and RNAs derived from transposable elements (repeat RNAs). RNA modifications of chromatin-associated RNAs, including m^6A and m^5C, serve as molecular signals that integrate RNA metabolism with chromatin regulation to control genome-wide transcription[32,33]. m^6A, deposited by METTL3 on promoter-associated, enhancer, and repeat RNAs, recruits nuclear readers such as YTHDC1 to promote RNA decay or facilitate interactions with chromatin-modifying complexes, thereby influencing histone marks, including H3K27ac and H3K9me3[32]. Similarly, m^5C on retrotransposon-derived caRNAs is recognized by methyl-CpG-binding proteins, such as MBD6, which directly deubiquitylates H2AK119ub to establish an open chromatin state, which is counteracted by TET2-mediated oxidation of m^5C[33]. Together, these modifications remodel chromatin architecture and fine-tune transcriptional programs across the genome.

Here, we revealed that m^1A modification of promoter-associated RNAs potentiates transcriptional elongation by facilitating RNA polymerase II release from promoter-proximal pausing sites at oncogenes, including MYC and glycolytic regulators. Paliperidone, a brain-penetrant dopamine D2 and 5-HT2A receptor antagonist used as an antipsychotic, inhibits TRMT61A activity, suppresses m^1A caRNA-dependent gene expression, and exerts combinatorial effects with ERBB family inhibitors. Together, these findings uncover a previously unrecognized transcriptional function of m^1A and provide a promising therapeutic strategy for GBM.

RESULTS

GSCs synthesize high rates of nascent RNA and display increased chromatin accessibility

RNAs associated with chromatin originate from nascent transcripts that are retained on open chromatin to modulate gene expression. To evaluate nascent RNA synthesis in GSCs relative to differentiated GBM cells (DGCs) and non-neoplastic neural stem cells (NSCs), we incubated the cells with the uridine analog 5-ethynyl uridine (EU) for 30 min. We detected transcripts incorporating EU by conjugating Alexa Fluor 488 via click chemistry to visualize the total nascent RNA. Fluorescence quantification revealed stronger EU signals in two patient-derived GSCs (GSC23 and GSC387) than in matched DGCs (DGC23 and DGC387) or NSCs (NSC11 and HNP1) (Fig. 1a, b), indicating a greater active transcriptional output in GSCs. To assess chromatin accessibility, we digested the exposed DNA using DNase I and employed labeling utilizing TUNEL to mark DNA regions within the open chromatin. Consistent with nascent RNA labeling, GSCs exhibited higher fluorescence intensities than DGCs or NSCs (Fig. 1c, d), suggesting that GSCs possess globally more relaxed chromatin that is conducive to active transcription. We then isolated the nuclei and directly extracted RNAs associated with chromatin for sequencing to profile the genomic distribution of caRNAs within GSCs, DGCs, and NSCs. Heatmap profiling of all genes encoding proteins corroborated that GSCs exhibited a greater abundance of caRNAs than DGCs and NSCs (Fig. 1e). Genome browser views of *OLIG1* and *OLIG2* loci showed caRNA signals predominantly detected in GSCs, where they colocalized with regions of high ATAC-seq accessibility and histone 3 lysine 27 acetyl (H3K27ac) enrichment (Fig. 1f). Integration of caRNA-seq, RNA-seq, ATAC-seq, and H3K27ac ChIP-seq data from GSC23 and GSC387 revealed that genes with high caRNA levels displayed a higher transcriptional output (Fig. 1g), stronger chromatin accessibility (Fig. 1h), and elevated H3K27ac signals (Fig. 1i) than those with intermediate or low caRNA abundance. These findings demonstrated that the abundance of caRNAs in GSCs is intrinsically linked to a chromatin environment that is permissible for active gene expression. Functional annotation showed that GSC-enriched caRNAs were preferentially associated with cell cycle-related genes, whereas DGC-derived caRNAs corresponded mainly to RNA processing genes, and NSC caRNAs were linked to neuronal activity genes (Extended Data Fig. 1a-c). Together, these results demonstrate that GSCs exhibit hyperactive chromatin landscapes that support the robust production of caRNAs, whose abundance reflects gene activation states and aligns with cell type-specific characteristics.

m^1A modification on caRNAs is elevated in GSCs

RNA modifications are increasingly recognized as key regulators of chromatin-associated RNAs. For instance, m^5C-modified caRNAs promote leukemia progression through epigenetic remodeling[33]. To determine which RNA modifications predominantly regulate caRNAs in GSCs, we profiled 55 known RNA modifications in purified caRNA fractions using liquid chromatography-tandem mass spectrometry (LC-MS/MS). Comparative analyses of GSCs, DGCs, and NSCs showed that N^1-methyladenosine (m^1A) was the most prominently elevated modification in GSC chromatin-associated RNAs, and this pattern was observed in both GSCs versus DGCs, and GSCs versus NSCs comparisons (Fig. 2a-d, Supplementary Table S1). Among the more than 100 chemically distinct RNA marks identified to date, N^1-methyladenosine (m^1A) has emerged as a dynamic and context-dependent modification that enhances oncogenic mRNA translation[34-36]. Crystallographic studies have revealed that m^1A disrupts canonical Watson-Crick base pairing and favors Hoogsteen interactions, thereby modulating the structural stability of loop-containing RNA motifs[37,38]. YTH domain-containing proteins, including YTHDF1-3 and YTHDC1[39], serve as readers that selectively recognize m^1A-modified RNAs, whereas the demethylases ALKBH1 and ALKBH3 function as erasers to reverse this modification[40,41]. Methodological advances in high-throughput sequencing have expanded the known landscape of m^1A, showing that it is not confined to tRNAs, mitochondrial RNAs, or rRNAs but also occurs in mRNAs, particularly near transcription start sites, suggesting broader regulatory roles[41-43].

To quantify the abundance of m^1A, we measured the absolute levels of m^1A and adenosine in purified caRNAs using LC-MS/MS. The m^1A-to-adenosine ratio in GSC caRNAs reached approximately 0.07% (Fig. 2e, f; Extended Data Fig. 2a-d). This quantitative analysis showed that GSCs contain higher m^1A levels than DGCs or NSCs. Dot blot assays using the m^1 A antibody confirmed the increased m^1A abundance in caRNAs from GSCs compared to DGCs and NSCs (Fig. 2g). In contrast, m^1A signals in mature mRNAs were barely detectable when equal amounts of RNA were loaded. Consistent with this observation, immunofluorescence staining of human GBM samples revealed strong nuclear m^1A signals co-localized with the stemness marker SOX2 (Extended Data Fig. 2e), whereas low-grade gliomas showed minimal levels of m^1A and SOX2 under identical imaging conditions (Extended Data Fig. 2f). To investigate the functional relevance of this modification, we analyzed 33 RNA modification

regulators across published genome-wide CRISPR screening datasets[44-47] which included GSCs, NSCs, and GBM cell lines (Extended Data Fig. 2g; Supplementary Table S2).

The m^1A writer complex, composed of TRMT6 and TRMT61A, catalyzes methylation at the N^1 position of adenine, typically within the T-loop of tRNAs, where m^1A58 stabilizes the tRNA architecture[48-50]. TRMT6 mediates RNA substrate recognition, whereas TRMT61A catalyzes methyl transfer[51]. Normalized quantitative Bayes factor (qBF) scoring identified the m^1A writer complex components TRMT6 and TRMT61A as essential for GSC survival (Fig. 2h). Immunoblotting revealed higher levels of the TRMT6/TRMT61A writer complex in GSCs than in DGCs and NSCs (Extended Data Fig. 2h). To directly test their role in nascent transcription, we performed a dual knockdown of TRMT6 and TRMT61A in GSCs using short hairpin RNAs (shRNAs). Thirty minutes of EU pulse labeling revealed that depletion of the TRMT6-TRMT61A complex reduced nascent RNA synthesis (Fig. 2i, j). Together, these findings demonstrate that TRMT6 and TRMT61A dependent m^1A modification are highly enriched in GSCs and support both caRNA accumulation and transcriptional activity.

SOX2 transcriptionally activates TRMT6 and TRMT61A

Given the upregulation of TRMT6 and TRMT61A in GSCs, we investigated the upstream molecular mechanisms that govern their expression. Examination of H3K27ac signals using a genome browser revealed that GSCs exhibited stronger H3K27ac enrichment at the promoters of TRMT6 and TRMT61A relative to NSCs (Extended Data Fig. 3a) and DGCs (Extended Data Fig. 3b). To identify potential transcriptional regulators, we correlated the expression of these methyltransferases with the top 20 transcription factors specific to GSCs[52] in the TCGA dataset. The master stemness factor, SOX2, was positively correlated with TRMT6 and TRMT61A (Extended Data Fig. 3c, d). To validate this relationship, we modulated SOX2 expression in GSCs. SOX2 knockdown decreased TRMT6 and TRMT61A mRNA and protein levels, whereas SOX2 overexpression induced their upregulation (Extended Data Fig. 3e, f). Chromatin immunoprecipitation confirmed direct SOX2 binding to the TRMT6 and TRMT61A promoter regions, with RNA Polymerase II serving as a positive control (Extended Data Fig. 3g). Collectively, these data indicate that SOX2 transcriptionally activates TRMT6

and TRMT61A in GSCs to elevate caRNA m^1A levels.

m^1A-modified caRNAs at promoter-proximal regions

To characterize the m^1A distribution within caRNAs, we transduced two GSCs with either a control non-targeting shRNA sequence (shCONT) or dual knockdown of TRMT6 and TRMT61A (shTRMT6/61A) to disrupt the formation of the functional TRMT6/61A methyltransferase complex, followed by caRNA isolation. We enriched m^1A modified caRNAs using an m^1A antibody and performed strand-specific library preparation, followed by sequencing after rRNA depletion (Fig. 3a). Sequencing data from two biologically independent replicates showed strong reproducibility for both GSC23 and GSC387 (Fig. 3b; Extended Data Fig. 4a, b). Representative genome tracks for oncogenes *MYC* and *PGK1* showed prominent m^1A deposition near transcriptional start sites (TSSs) (Fig. 3c). In MYC, m^1A signals also extended across the gene body, suggesting a potentially broader regulation. Analysis of the m^1A peaks identified in GSC387 and GSC23 revealed that the m^1A peaks on caRNAs were predominantly enriched near TSSs (Fig. 3d). De novo motif analysis showed that these peaks were localized mainly within adenine-rich sequences characterized by an AANAA motif (Extended Data Fig. 4c). Annotation of the overlapping peaks identified in GSC23 and GSC387 revealed 3,050 m^1A-modified caRNA peaks (Fig. 3d). Heatmap analysis demonstrated that TRMT6 and TRMT61A knockdown reduced the m^1A signals at the identified peaks, indicating that these modifications are dependent on the TRMT6/61A complex (Fig. 3e).

The m^1A enrichment near the TSSs suggests that the writer complex might operate directly on chromatin. Immunofluorescence analyses of endogenous TRMT6 and TRMT61A in GSCs revealed that both subunits were localized mainly to the nucleus, with additional weaker cytoplasmic signals (Extended Data Fig. 4d). To validate chromatin engagement, we fractionated the GSCs into cytoplasmic, nucleoplasmic, and chromatin compartments. Western blotting confirmed that both subunits were associated with the chromatin fraction (Extended Data Fig. 4e). Next, we profiled the genome-wide occupancy of TRMT6 and TRMT61A using ChIP-seq. A total of 7,867 protein-coding genes were identified as TRMT6/61A bound genes, and heatmap analyses showed that both enzymes

were strongly enriched at TSSs (Fig. 3f), consistent with the promoter-proximal accumulation of m^{1}A-containing caRNAs observed by RNA immunoprecipitation followed by deep sequencing (RIP-seq). Genome browser tracks at representative loci, such as *MYC* and *PGK1*, illustrated that TRMT6 and TRMT61A co-occupied promoter regions, together with active chromatin signatures and RNA polymerase II, whereas repressive histone marks were absent (Fig. 3g).

Peak-overlap analyses showed that most TRMT6/61A peaks coincided with RNA polymerase II peaks, with more than 60% located near promoter regions (Extended Data Fig. 4f, g). Motif analysis revealed that TRMT6 and TRMT61A preferentially bound A-rich promoter sequences (Extended Data Fig. 4h), consistent with the enrichment of AANAA motifs in our RIP-seq data. Peak annotation demonstrated extensive co-occupancy with RNA polymerase II, including its Ser2- and Ser5-phosphorylated forms, as well as with accessible chromatin (ATAC-seq), H3K27ac, and histone 3 lysine 4 trimethyl (H3K4me3), but not with repressive histone marks H3K9me3 or H3K27me3 (Extended Data Fig. 5a). Genes bound to TRMT6/61A exhibited higher transcriptional activity than non-bound genes (Extended Data Fig. 5b). Inhibition of transcriptional elongation by a CDK9 inhibitor reduced TRMT6/61A chromatin occupancy (Extended Data Fig. 5c), supporting a transcription-coupled recruitment mechanism.

Given that N^6-methyladenine (6mA) can occur in DNA and is influenced by RNA methyltransferases in certain contexts[53-56], we examined whether TRMT6/61A binding to chromatin in GSCs could generate DNA N^1-methyladenine (m^{1}dA). LC-MS/MS profiling of nucleotides from the digested GSC387 genomic DNA did not detect m^{1}dA above the background (Extended Data Fig. 5d-g). These data indicate that TRMT6/61A does not modify DNA at the N^1 position but instead regulates transcriptional programs through m^{1}A installation on nascent caRNAs. Together, these findings suggest that the TRMT6/61A complex recognizes A-rich promoter DNA and installs m^1 A on nascent promoter-associated caRNAs to sustain transcriptional output.

caRNA m^{1}A maintains MYC-driven transcription

Beyond its canonical functions, m^1A exerts its effects in a disease-associated context. It promotes the expansion of CAG repeat RNAs and facilitates their direct binding to TDP-43, triggering cytoplasmic mislocalization and the formation of gel-like aggregates, reminiscent of those observed in neurodegenerative disorders[36]. In hematopoietic stem cells, TRMT6 and TRMT61A noncanonically induce biogenesis of 3′-tiRNA-Leu-CAG, thereby impairing self-renewal and compromising hematopoietic homeostasis[57]. Collectively, m^1A selectively modulates RNAs with intricate secondary structures and mediates pathological outcomes in diverse biological systems. To assess the transcriptional consequences of m^1A loss, we integrated m^1A-modified caRNA targets identified by m^1A RIP-seq with the TRMT6/TRMT61A-bound genes identified by ChIP-seq (Fig. 4a). This analysis identified 1,727 overlapping genes, which were examined by RNA sequencing after TRMT6 and TRMT61A depletion. Differential expression analysis of these 1,727 m^1A-marked and TRMT6/TRMT61A-bound genes revealed that 569 genes were downregulated, including MYC, whereas only 112 genes were upregulated (Fig. 4b). Therefore, we defined these 569 downregulated genes as core m^1 A regulated genes. Gene Ontology analysis showed that these core m^1A-regulated genes were enriched for canonical MYC target genes, as well as genes involved in cell cycle progression and glycolysis, indicating that m^1A modification of caRNAs is required to sustain oncogene-associated transcriptional programs (Fig. 4c).

Next, we designed gRNAs targeting the MYC caRNA at its TSS and generated Tet-On inducible fusion constructs linking the dRfxCas13d protein to either wild-type ALKBH3 or a catalytically inactive mutant (Fig. 4d)[43,58]. Doxycycline induction resulted in a time-dependent increase in fusion protein expression, as confirmed by immunoblotting (Fig. 4e). MYC mRNA and protein levels progressively declined upon recruitment of the wild-type ALKBH3, whereas the catalytic mutant induced minimal changes (Fig. 4f). m^1 A RIP-qPCR confirmed that m^1 A modified MYC caRNA but not mature MYC mRNA, and ALKBH3 expression reduced the enrichment of MYC caRNA (Fig. 4g). Loss of m^1A decreased MYC caRNA stability, suggesting that m^1A maintained MYC caRNA abundance (Fig. 4h). As m^1 A loss can affect protein translation, we used transient siRNA-mediated knockdown of TRMT6 and TRMT61A to assess m^1A-dependent regulation of MYC mRNA and found that TRMT6/61A depletion reduced MYC mRNA within 48 h before marked protein loss, followed by decreased MYC protein expression

(Extended Data Fig. 6a, b). Consistent with these findings, TCGA data analysis showed that TRMT6/61A expression was positively correlated with both MYC expression and the Hallmark MYC target signature (Extended Data Fig. 6c, d). Together, these data indicated that TRMT6/61A-mediated m^1A deposition on caRNAs is essential for maintaining MYC expression.

Loss of caRNA m^1A impairs Pol II pause-release and elongation

To determine how caRNA m^1A influences transcription, we depleted TRMT6 and TRMT61A in GSCs and performed RNA Pol II ChIP-seq, focusing on the m^1A-marked and TRMT6/TRMT61A-bound genes identified by integrated m^1A RIP-seq and ChIP-seq analyses (Fig. 4a). Metagene profiling revealed a distinct accumulation of RNA Pol II at the TSSs upon TRMT6/61A knockdown (Fig. 5a). As elevated promoter-proximal Pol II signals often reflect transcriptional pausing[59-61], we calculated the pausing index (ratio of reads within ±200 bp of the TSS to reads across the gene body)[62]. TRMT6/61A depletion caused a rightward shift in the pausing index distribution (Fig. 5b), indicating an enhanced promoter-proximal pausing. Productive transcriptional elongation requires Ser2 phosphorylation (Ser2P) of RNA Pol II by P-TEFb. For representative genes, such as *MYC* and *PKM*, TRMT6/61A loss increased Pol II accumulation at the TSS while diminishing Ser2P signals across gene bodies in both GSC23 and GSC387 cells (Fig. 5c). Heatmaps centered on TSSs showed increased promoter-proximal RNA Pol II densities in genes marked by caRNA m^1A (Fig. 5d). ChIP-seq profiling of RNA Pol II Ser2P revealed reduced Ser2P occupancy across gene bodies following TRMT6/61A knockdown (Fig. 5d), indicating impaired elongation. To validate these observations, we performed 4-sU metabolic labeling of nascent RNA for 15 min in the presence or absence of TRMT6/61A (Extended Data Fig. 6e). Pulldown of newly synthesized RNA followed by qPCR revealed reduced nascent transcript levels of glycolytic genes such as *GLUT1*, *PKM*, and *PGK1* (Fig. 5e), previously identified as m^1A-modified targets, supporting a defect in transcriptional elongation. We used our Tet-On inducible system to remove m^1A from the *MYC* promoter-proximal caRNA to assess the impact of m^1A on transcription elongation at the single-gene level. ChIP-qPCR demonstrated increased RNA Pol II occupancy at the *MYC* TSS (Extended Data Fig. 6f) accompanied by a reduction in newly synthesized *MYC* mRNA (Extended Data Fig. 6g).

Next, we performed RNA pull-down assays using m^{1}A-modified and unmodified MYC caRNA oligonucleotides incubated with nuclear proteins from GSC387, followed by mass spectrometry to investigate how caRNA m^{1}A regulates transcriptional elongation. YTHDC1, a known m^{1}A reader, and other RNA-binding proteins were identified (Fig. 5f, Supplementary Table S3). Among the top enriched RNA-binding proteins, SETX has recently been reported to associate with RNA transcription complexes and to regulate transcriptional elongation[63]. Western blot validation confirmed that m^{1}A-modified MYC caRNA preferentially pulled down SETX, RNA Pol II, CDK9, and components of the NELF and super-elongation complex (Fig. 5g). ChIP-qPCR showed that SETX occupied the MYC promoter-proximal region, whereas TRMT6/TRMT61A knockdown, which reduced caRNA m^{1}A, impaired SETX occupancy at this locus (Fig. 5h). TCGA analysis revealed that SETX expression was positively correlated with core m^{1}A-regulated gene signature and MYC expression (Fig. 5i, j). Together, these results support a role for SETX in linking caRNA m^{1}A to Pol II pause release and productive transcriptional elongation.

Depletion of TRMT6 and TRMT61A impairs glycolysis

To evaluate the functional consequences of TRMT6/61A depletion in GSCs, we used our RNA-seq data for downstream analysis. In GSC387 cells, two independent shRNAs produced 2,162 overlapping downregulated genes and 2,110 upregulated genes (Fig. 6a, b). Gene ontology analyses revealed that the loss of TRMT6/61A suppressed glycolytic pathways and MYC-regulated programs (Fig. 6c). We selected five curated glycolysis-related gene sets from the Biocarta, Hallmark, KEGG, Reactome, and WP pathway databases, and performed GSEA on both shRNA datasets. All five gene sets showed negative enrichment after TRMT6/61A knockdown (Fig. 6d). qPCR validated the reduction in expression of representative glycolytic genes (Fig. 6e). Given that transcriptional repression of these genes often reflects impaired glycolytic function, we measured lactate secretion and glucose uptake, and observed clear reductions in both, indicating a glycolytic defect in TRMT6/61A-deficient GSCs (Fig. 6f). Seahorse analyses demonstrated a diminished glycolytic capacity relative to that of control cells (Fig. 6g). For the TRMT6/61A-dependent upregulated genes, gene ontology analyses revealed strong enrichment for the interferon-gamma and inflammatory response pathways (Extended Data Fig. 7a). Representative genes were validated using qPCR (Extended Data Fig. 7b). Analysis of TCGA GBM

datasets showed that TRMT6/61A expression was negatively correlated with infiltration of cytotoxic T cells, CD4 T cells, macrophages, and dendritic cells (Extended Data Fig. 7c). Taken together, these findings indicate that inhibiting TRMT6/61A simultaneously attenuates tumor cell glycolysis while inducing a tumor-intrinsic inflammatory response, highlighting its potential as a therapeutic target.

Paliperidone targets TRMT61A and inhibits tumor progression

The regulatory interplay among TRMT6/61A, caRNA m^1A, and glycolytic programs suggests that TRMT6/61A supports GSC growth. To examine cellular phenotypes, we selected three patient-derived GSCs and established a stable knockdown of TRMT6/61A using two independent shRNAs (Fig.7a). TRMT6/61A depletion impaired GSC proliferation, as reflected by reduced growth rates (Fig. 7b). Self-renewal was also diminished, as evidenced by smaller tumor spheres (Fig. 7c) and reduced stem cell frequency in extreme limiting dilution assays (Fig. 7d, Extended Data Fig. 8a). In vivo tumorigenicity assays demonstrated that loss of TRMT6/61A attenuated tumor size progression, as demonstrated by attenuated bioluminescent signals and prolonged survival in the two orthotopic xenograft models (Fig. 7e, f).

To assess the clinical relevance of TRMT6/61A-regulated caRNA m^1A, we compiled the top 50 m^1A-modified genes that overlapped between GSC23 and GSC387 cells and used them as an m^1A signature. In both the CGGA and TCGA GBM datasets, higher signature expression predicted unfavorable patient outcomes (Extended Data Fig. 8b, c). Given that the TRMT6/TRMT61A complex is required for the maintenance of the GSC transcriptional program and is more highly expressed in tumor cells than in normal immune cells or oligodendrocytes (Extended Data Fig. 8d), yet no selective TRMT6/TRMT61A inhibitors are currently available, we sought to identify potential pharmacological inhibitors of this complex. Because the crystal structure of the TRMT6/TRMT61A complex is available, we performed a structure-based docking screen using FDA-approved compounds to identify clinically translatable candidates that may target the catalytic subunit TRMT61A (Fig. 7g, Supplementary Table 4). The compounds were docked against the predicted SAM/SAH-binding pocket of TRMT61A. Among the top 20 compounds ranked by docking score, paliperidone palmitate, a dopamine D2 receptor, and 5-

hydroxytryptamine 2A receptor antagonist, clinically used as an anti-psychotic, emerged as brain-penetrant candidates. Docking analysis predicted that paliperidone palmitate occupied the SAH-binding pocket of TRMT61A, suggesting that it may interfere with TRMT61A methyltransferase activity (Fig. 7h, Extended Data Fig. 8e). As paliperidone palmitate is a prodrug that is hydrolyzed to free paliperidone after cellular uptake, we examined whether paliperidone directly interacts with TRMT61A. Surface plasmon resonance analysis of purified TRMT61A demonstrated direct binding between paliperidone and TRMT61A (Fig. 7i). Cellular thermal shift assays showed that paliperidone increased TRMT61A thermal stability (Extended Data Fig. 8f), supporting target engagement in cells. Paliperidone treatment suppressed the growth of GSCs, whereas differentiated glioma cells and normal neural stem cells were less sensitive to paliperidone (Fig. 7j). Consistent with these findings, paliperidone reduced the m^1A levels in chromatin-associated RNA and decreased the expression of MYC and glycolysis-related genes, producing effects similar to those observed following TRMT6/TRMT61A depletion (Fig. 7k, Extended Data Fig. 8g). These findings demonstrate that TRMT6/TRMT61A-mediated caRNA m^1A is essential for maintaining GSC identity and tumor propagation and that paliperidone binds TRMT61A and suppresses caRNA m^1A, highlighting the TRMT6/TRMT61A–caRNA m^1A axis as a potential therapeutic target in GBM.

Paliperidone sensitizes GSCs to ERBB inhibition

To explore the potential clinical relevance of TRMT6/TRMT61A-dependent m^1A activity in GBM therapy, we analyzed the association between the core m^1A-regulated gene signature and drug response using DepMap pharmacogenomic datasets. High expression of the m^1A signature was positively associated with resistance to ERBB/HER family inhibitors, suggesting that elevated TRMT6/TRMT61A-m^1A activity may contribute to reduced sensitivity to EGFR/HER-targeted therapies (Fig. 8a). Among these inhibitors, poziotinib showed one of the strongest associations with the m^1A signature and was therefore selected for further investigation (Extended Data Fig. 8h). Previous work has shown that poziotinib penetrates the blood–brain barrier and inhibits brain metastases, supporting its potential relevance in brain tumor therapy[64].

Combined treatment with paliperidone and poziotinib increased the sensitivity of GSCs to poziotinib, as reflected by a reduction in poziotinib IC_{50} (Fig. 8b, c). Next, we evaluated the therapeutic efficacy of this combination in a GSC387 xenograft model. As shown in Fig. 8d, mice bearing xenograft tumors were treated beginning on day 7 after implantation for two weeks, followed by the monitoring of tumor growth and survival. Compared to either single-agent treatment, the combination of paliperidone and poziotinib more effectively suppressed GSC tumor growth and extended the survival of recipient mice (Fig. 8e-g). Taken together, these findings indicate that paliperidone suppresses the TRMT61A-dependent caRNA m^1A signature and sensitizes GBM cells to poziotinib treatment, thereby inhibiting glioma growth in vivo.

DISCUSSION

Chromatin-associated RNAs represent an emerging regulatory layer in transcriptional control[29,65]. They arise co-transcriptionally and remain tethered to chromatin, where they influence promoter activity, modulate transcription factor recruitment, and contribute to the transition from initiation to productive elongation, in part by recruiting cofactors such as Tip60, p400, and P-TEFb[66,67]. Although the functional roles of m^6A and m^5C have been extensively characterized, the landscape of RNA modifications operating at the chromatin interface remains comparatively underexplored. In this study, we delineated a regulatory mechanism governed by the N^1-methyladenosine writer complexes TRMT6 and TRMT61A. We showed that m^1A functions as a regulatory node that promotes the release of RNA Polymerase II from promoter-proximal pausing and drives productive transcriptional elongation of oncogenes such as MYC and metabolic regulators including PGK1 and PKM through SETX (Fig. 8h). Reduced MYC activity may reinforce the suppression of glycolytic gene expression, as MYC is a master transcriptional regulator of glycolysis in tumor cells. Virtual drug screening of an FDA-approved compound library identified paliperidone as a candidate inhibitor of TRMT61A and the caRNA m^1A signature. Moreover, paliperidone combined with the ERBB family inhibitor poziotinib suppressed GSC xenograft progression. These findings expand the functional repertoire of m^1 A beyond its canonical roles in translation and establish a mechanism of transcriptional control that is essential for sustaining GSC programs.

The transition of RNA Polymerase II from a promoter-proximal paused state to productive elongation represents a major rate-limiting step in gene expression[60,61,68]. Although phosphorylation of the C-terminal domain of RNA Polymerase II by P-TEFb[69,70], often in cooperation with the Super Elongation Complex[71-73], constitutes the canonical trigger for pause release, our findings indicate that modification of the nascent RNA introduces an additional regulatory layer. We observed that depletion of the m^1A writer complex led to substantial accumulation of RNA Polymerase II at transcription start sites, accompanied by a reduction in Ser2 phosphorylation across gene bodies. These results suggest that m^1A deposition facilitates the transition from pausing to elongation, possibly by alleviating the structural impediments that hinder polymerase progression. The presence of a methyl group at the N^1 position of adenine disrupts canonical Watson-Crick base pairing and

414 introduces a positive charge[74-76], which may influence the folding of the nascent transcript. We
415 speculate that this chemical alteration could recruit RNA-binding proteins, such as SETX, that promote
416 the engagement of elongation factors. These interpretations align with emerging evidence that co-
417 transcriptional RNA processing plays a direct role in shaping the transcriptional dynamics. Together,
418 our data support a model in which the regulatory information that governs transcriptional output is
419 encoded not only in chromatin modifications but also directly on nascent RNA as it emerges from the
420 polymerase.

421

422 The biological function of m^1A is highly context dependent. In the cytoplasm, m^1A is best
423 characterized at position 58 or 9 of tRNAs, where it contributes to stabilization of the canonical tRNA
424 tertiary structure and supports translational fidelity[50,77]. In the context of DNA, N^1 methyladenine
425 (m^1dA) is typically regarded as a toxic lesion induced by alkylating agents that blocks replication and
426 requires repair by enzymes, such as ALKBH2[78]. However, our mass spectrometry analysis of genomic
427 DNA from GSCs showed no detectable m^1dA signal, confirming that the TRMT6 and TRMT61A
428 complex functions exclusively as an RNA methyltransferase. GSCs repurpose the conserved tRNA
429 modification machinery to perform a non-canonical function in the nucleus. While m^1A in the 5'
430 untranslated region (UTR) of mature mRNA has been reported to enhance translation initiation, our
431 discovery of m^1A in nuclear RNAs associated with chromatin establishes a role upstream of translation.
432 This suggests that the same chemical mark conveys different instructions depending on the RNA
433 species and subcellular localization. In GSCs, the nuclear fractions of TRMT6 and TRMT61A are not
434 redundant but rather a specialized population dedicated to sustaining the high transcriptional
435 demand of the stem cell state. Another tRNA modification, ac4C, has also been implicated in
436 transcriptional regulation of chromatin-associated tRNAs and R-loop RNAs, where it can modulate
437 histone modification states and promote transcription[23,79]. Together, these studies suggest that RNA
438 modifications of tRNAs and other chromatin-associated RNAs may constitute a broader regulatory
439 layer that links classical RNA-modifying enzymes to chromatin-dependent gene expression.

440

441 Previous work has shown that tRNA m^1A58 modification supports efficient MYC protein synthesis

during T-cell activation[35]. Our findings demonstrate that m^1A also operates at the transcriptional level through modification of promoter-associated chromatin-bound RNAs, which introduces an additional regulatory layer into the complex hierarchy controlling MYC expression. We showed that TRMT6 and TRMT61A are direct transcriptional targets of SOX2 and that these enzymes sustain MYC output by enabling efficient elongation of its nascent transcript. In addition to MYC, our data revealed that m^1A regulated the transcription of glycolytic genes. The reprogramming of glucose metabolism is a hallmark of malignancy and is often attributed to the enhanced expression of metabolic enzymes. A previous study identified an m^1A site in ATP5D mRNA that restrained translation elongation, whereas targeted demethylation increased ATP5D expression and glycolytic activity in Hela cells[80]. In contrast, our work on GBM showed that m^1A modifies the nascent chromatin-associated RNAs of glycolytic genes, such as PGK1 and PKM, and promotes their transcription directly. This observation indicates that tumor cells employ m^1A through distinct mechanisms, namely, translational regulation via tRNA and transcriptional regulation via chromatin-associated RNA, to coordinate metabolic reprogramming.

Pharmacological targeting of RNA-modifying enzymes is becoming increasingly feasible. The selective METTL3 inhibitor STM2457 provides a proof-of-concept that pharmacological inhibition of an RNA methyltransferase can suppress tumor growth in preclinical models[22], and the METTL3 inhibitor STC-15 has subsequently advanced from first-in-human Phase I evaluation to Phase II clinical development[81], with evidence of pharmacodynamic target engagement and early antitumor activity. Therefore, the identification of paliperidone, an FDA-approved CNS-active drug, as an inhibitor of TRMT61A, provides a potential drug-repurposing strategy for GBM. However, given the established pharmacological activity of paliperidone at dopamine and serotonin receptors[82], further studies are required to define its selectivity for TRMT61A, determine the therapeutic window for m^1A inhibition, and develop more selective compounds targeting this pathway. Our observation that paliperidone enhances the antitumor activity of the ERBB family inhibitor poziotinib further suggests that targeting the m^1A-dependent transcriptional program may be particularly effective in combination with inhibitors of oncogenic signaling pathways.

In summary, our study revealed an essential epitranscriptomic axis in GBM, where SOX2 drives the expression of TRMT6 and TRMT61A. This complex localizes to the nucleus to install m^1A on RNAs associated with chromatin proximal to promoters. This modification acts as a critical regulator of transcriptional elongation and orchestrates the expression of oncogenic and glycolytic proteins. By connecting RNA modifications directly to the machinery of gene transcription, we provide a new paradigm for understanding how cancer cells maintain their identity, and identify the m^1A writer complex as a promising target for disrupting the transcriptional addiction of GBM.

METHODS

GSC derivation and cell culture

Human GBM specimens were obtained from patients undergoing surgical resection at Duke University and University Hospital Cleveland Medical Center. Tissue acquisition was performed with written informed consent under an institutional review board–approved protocol (#090401) and in accordance with the ethical guidelines. After the neuropathological evaluation, surplus surgical material not required for clinical diagnosis was retained for research purposes. Patient-derived xenografts (PDXs) were used as renewable sources of GBM stem cells (GSCs) to minimize the artifacts associated with long-term in vitro culture. The GSC23 and GSC387 lines were derived from a recurrent GBM biopsy of a 63-year-old male patient (kindly provided by Dr. Erik Sulman, NYU Langone Health) and from a primary GBM of a 76-year-old female patient. GSC3028 was derived from a recurrent GBM from a 65-year-old female patient, and GSC468 was derived from a GBM sample transferred to our laboratory through a material transfer agreement with the Case Western Reserve University. Non-malignant neural stem cell (NSC) controls included NSC11 (ALSTEM) derived from human induced pluripotent stem cells (hiPSCs), and HNP1 (Neuromics Biosciences) generated from WA09-derived hiPSCs. All GSC and NSC lines were cultured in Neurobasal medium (Thermo) supplemented with B27 minus vitamin A (Thermo), 20 ng/mL EGF (R&D Systems), 20 ng/mL bFGF (R&D Systems), sodium pyruvate (Thermo), GlutaMAX (Thermo), and penicillin–streptomycin (Thermo). Differentiated glioma cells (DGCs) were generated by culturing GSCs in DMEM (Gibco) containing 10% fetal bovine serum (Gibco) for ≥7 days to induce phenotypic transition. HEK293T cells (ATCC) were maintained in DMEM with 10% FBS under 37 °C, 5% CO_2, and 20% O_2. All GSC cultures were used within 20 passages of xenograft recovery. Short tandem repeat (STR) profiling was performed annually to authenticate cell identity, and *mycoplasma* contamination was routinely monitored using PCR analysis.

Xenograft models

All mouse experiments were conducted in accordance with the guidelines of the Institutional Animal Care and Use Committee of the University of Pittsburgh (Protocol #21049014). Mice were maintained under specific-pathogen-free conditions at an ambient temperature of 20–26 °C, relative humidity of

30–70%, and a 12-hour light/dark cycle. Male and female mice were used in this study. For intracranial xenograft experiments, healthy BALB/c-nu nude mice aged 4–6 weeks were randomly selected and injected with 10,000 GSC cells into the right cerebral cortex at a depth of 3.5 mm following standard stereotaxic procedures. For the paliperidone and poziotinib combination experiment, mice were randomized into four treatment groups seven days after GSC387-luciferase cell implantation, with six mice per group. Paliperidone was administered by intraperitoneal injection at 3 mg/kg once daily for 2 weeks. Poziotinib was administered by oral gavage (2 mg/kg) five times per week for two weeks. Mice in the combination group received both paliperidone and poziotinib according to the dosing schedule described above. All the animals were housed and monitored under controlled conditions by a licensed veterinarian to ensure welfare and consistency. The mice were observed daily and euthanized at the onset of neurological symptoms, including hunched posture, altered gait, lethargy, or significant weight loss. Mouse brains implanted with firefly luciferase-labeled GSCs were monitored using bioluminescence imaging. Animals were intraperitoneally treated with d-luciferin (50 mg/kg, Promega) and anesthetized with isoflurane for imaging analysis. Bioluminescent images were captured using an IVIS imaging system (PerkinElmer). Survival curves were generated using GraphPad Prism software, and statistical significance was determined using the log-rank (Mantel–Cox) test.

Click-iT EU Nascent RNA labeling Assay

The nascent RNA synthesis assay was performed using the Click-iT RNA Alexa Fluor 488 Imaging Kit (Invitrogen) according to the manufacturer's instructions. 5-Ethynyl uridine incubation was performed for 30 min before washing with the cell medium. The cell nuclei were counterstained with Hoechst 33342 (Abcam). Samples were imaged using a Leica SP8 laser scanning confocal microscope at the University of Pittsburgh. The fluorescence intensity across different samples was quantified using the ImageJ software.

Chromatin accessibility detection with DNase I based TUNEL system

GSC, DGC, and NSC were seeded to 12 wells plate on Matrigel-coated coverslips 12 h before detection.

The DNase I-TUNEL assay was performed using the DeadEnd Fluorometric TUNEL System (Promega), according to the manufacturer's instructions, after fixation with paraformaldehyde and permeabilization with Triton X-100. Cells were treated with 1 U/ml of DNase I (Thermo Fisher Scientific) for 5 min at 37 °C before rTdT labeling. Samples were imaged using a Leica SP8 laser scanning confocal microscope at the University of Pittsburgh. The fluorescence intensity across different samples was quantified using the ImageJ software.

Immunofluorescence staining

For immunofluorescence analysis, cells were grown on Matrigel-coated coverslips and fixed with 4% PFA for 15 min, followed by permeabilization with 0.1% Triton X-100 in PBS for 15 min. After washing three times with PBS, cells were blocked in PBS buffer with 5% goat serum for 1 h. The relevant primary antibodies diluted in blocking buffer were then incubated at 4 °C overnight, followed by incubation with secondary antibodies for 1 h at room temperature, according to manufacturer's instructions. Tumor-bearing brain tissues were permeabilized and blocked in PBS buffer with 0.1% Triton X-100 and 5% goat serum. The sections were then incubated with primary antibodies at 4 °C overnight and appropriate secondary antibodies for 1 h at room temperature. The samples were imaged using a Leica SP8 laser scanning confocal microscope.

Lentiviral transduction

Lentiviral clones expressing short hairpin RNAs (shRNAs) targeting TRMT6, TRMT61A, or SOX2 were obtained from Sigma-Aldrich. A non-targeting control shRNA encoding a sequence that is not present in the mammalian genome (shCONT) was cloned into the pLKO.1 vector. Single-guide RNAs targeting MYC (sgMYC) was cloned into the RfxCas13d backbone. Lentiviral Tet-On overexpression plasmids encoding NLS-dRfxCas13d fused to ALKBH3 or catalytically inactive dALKBH3 and the lentiviral overexpression plasmid SOX2 were ordered from VectorBuilder. Lentiviral particles were produced in HEK293T cells by co-transfection of lentiviral plasmids with packaging vectors pCMV-dR8.2 dvpr and pCI-VSVG. The viral supernatants were collected and concentrated using a Lenti-X Concentrator (Takara Bio) according to the manufacturer's instructions. Target cells were transduced with lentivirus

for 24 h, followed by a 24 h recovery period before selection. Infected cells were selected using puromycin until all uninfected control cells were eliminated.

RNA-Seq and data analysis

Total RNA was extracted from 50 million GSC using TRIzol reagent (Thermo Fisher Scientific) and purified using the Direct-zol RNA Miniprep Kit (Zymo Research), following the manufacturer's protocols. Library construction was performed using the NEBNext Ultra RNA Library Prep Kit for Illumina (Novogene). The resulting RNA-Seq libraries were sequenced using 150 bp paired-end reads on a NovaSeq 6000 platform. Raw FASTQ reads were trimmed and aligned to the human reference genome (hg38) using HISAT2 (v2.1.0)[83]. Read counts for the specified regions were quantified with HTSeq-count (v0.12.3)[84] and analyzed for differential gene expression using DESeq2 (v1.32.0)[85] with a paired model in the two cell lines. An adjusted P value < 0.05, and $|\log_2$ fold change$| \geq 0.5$, were used to identify differentially expressed genes. GO enrichment analysis was performed using Metascape (https://metascape.org) and visualizations were generated using the ggplot2 package in R [86]. For Gene Set Enrichment Analysis, gene signatures in the gmt format were downloaded from the GSEA Database (https://www.gsea-msigdb.org/), and enrichment analysis was performed using the GSEABase package in R.

Chromatin immunoprecipitation (ChIP) sequencing and data analysis

GSC cells with or without TRMT6/61A knockdown were crosslinked with 1% paraformaldehyde for 10 min and quenched with glycine for 5 min. After cell lysis, the fixed chromatin was sonicated to generate DNA fragments ranging from 200 to 600 bp using a Sonics Vibra-Cell Processor VCX130. DNA fragments were immunoprecipitated using specific antibodies and Protein A/G magnetic beads (Sigma-Aldrich). Between 1 and 10 ng of immunoprecipitated DNA was used for library preparation with the NEBNext Ultra DNA Library Prep Kit for Illumina sequencing at Novogene. Raw ChIP-Seq reads were trimmed and aligned to the human reference genome (hg38) using Bowtie[87] with the default parameters. Read coverage was calculated using the bamCoverage command in deepTools[88] and normalized to counts per million (CPM). Heatmaps and metagene profiles were generated using

590 the computeMatrix function in DeepTools. De novo motif enrichment was performed using the
591 MEME[89] suite by analyzing FASTA sequences derived from the binding peaks of TRMT6 and TRMT61A.
592 Genomic annotation of these peaks was conducted using the ChIPseeker[90] package in R. Finally,
593 visualization of sequencing signals in the BigWig format was carried out using Integrative Genomics
594 Viewer[91].

595

596 **Chromatin associated RNA Sequencing and data analysis**

597 To obtain chromatin-associated RNA, the precipitation method was used, as previously described with
598 modificatoins[33,92]. Briefly, 10 million GSC were harvested and washed twice with 10 ml of ice-cold PBS.
599 Cells were lysed on ice for 10 min in cell lysis buffer (10 mM Tris-HCl pH 8.0, 10 mM NaCl, 85 mM KCl,
600 0.5% NP-40). Nuclear pellets were resuspended in 400 µl of cold glycerol buffer (10 mM HEPES pH
601 7.9, 100 mM KCl, 0.1 mM EDTA, 10% glycerol, 1 mM DTT) supplemented with RNase inhibitor,
602 followed by vortexing. An additional 400 µl of cold 2× NUN buffer (25 mM HEPES pH 7.9, 300 mM
603 NaCl, 1 M urea, 1% NP-40) was added, and the mixture was vortexed and incubated on ice for 10 min.
604 Chromatin pellets were collected by centrifugation at 14,000 rpm for 2 min at 4 °C, then washed four
605 times with 1× NUN buffer. The chromatin pellet was lysed in 1 ml of TRIzol reagent and heated to
606 65 °C to dissolve chromatin. RNA was extracted according to the manufacturer's instructions. To
607 remove free mRNA, the extracted RNA was incubated with oligo (dT)25 magnetic beads (NEB)
608 followed by treatment with RNase-free DNase I to eliminate residual mRNA and genomic DNA. RNA
609 was purified using VAHTS RNA Clean Beads (Vazyme). The collected chromatin-associated RNA was
610 subjected to library construction using the NEBNext Ultra II Directional RNA Library Prep Kit for
611 Illumina at Novogene. Sequencing reads were aligned to the human reference genome (hg38) using
612 HISAT2.

613

614 caRNA m^1A RIP was performed using the EpiQuik CUT & RUN RNA Enrichment (MeRIP) Kit (Epigentek)
615 and anti-m^1A antibody (MBL) on caRNA extracted using the method described above. The enriched
616 RNA was then subjected to ribosomal RNA depletion using the NEBNext rRNA Depletion Kit v2,
617 followed by library preparation using the NEBNext Ultra II Directional RNA Library Prep Kit for Illumina,

performed at Novogene. Sequencing reads were processed with fastp[93] to remove adapter sequences and were aligned to the human reference genome (hg38) using HISAT2. To identify genes containing m1A caRNA, MACS2[94] was used for peak calling using the default parameters and a q-value cutoff of 0.01. For visualization, read coverage was normalized to counts per million (CPM) using deepTools and displayed in the IGV.

Quantitative analysis of m^1A using mass spectrometry analysis

Chromatin-associated RNA samples were quantified using the Qubit RNA High Sensitivity (HS) Assay Kit (Thermo Fisher Scientific), according to the manufacturer's instructions, to ensure accurate RNA concentration measurements prior to downstream analysis. RNA and genomic DNA samples were enzymatically hydrolyzed into single nucleosides using the Nucleoside Digestion Mix (New England Biolabs). The resulting nucleoside solutions were subsequently deproteinized using a 10,000-Da molecular weight cut-off (MWCO) centrifugal filter (Sartorius). Nucleoside mixtures were analyzed using an Agilent 6460 triple quadrupole (QQQ) mass spectrometer coupled to an Agilent 1260 HPLC system. Data were acquired in the multiple reaction monitoring (MRM) mode, which provides high sensitivity and selectivity for the detection of modified nucleosides based on specific parent-to-product ion transitions. LC–MS data were acquired and processed using Agilent Qualitative Analysis software. MRM chromatographic peaks corresponding to individual modified nucleosides were extracted and quantified, and the peak areas were normalized to the amount of injected chromatin-associated RNA to enable comparisons across samples. To quantify m^1A in caRNA and m^1dA in DNA, a Waters Synapt G2-Si Q-TOF mass spectrometer coupled to a Waters Acquity H-Class UPLC system was used. Data were acquired in the high-resolution mode. LC–HR-MS data were collected using Waters MassLynx 4.2 software and processed with TargetLynx. Quantification was performed by comparison with standard curves generated from pure nucleoside standards analyzed in parallel within the same batch.

Transient transcriptome qPCR (TT-qPCR)

TT-qPCR was performed as previously described with a few modifications[95]. Briefly, nascent RNA was

646 labeled with 4sU (0.5 mM; Sigma) for 15 min at 37 °C in cells. Cell nuclei were isolated with CE buffer
647 (Hepes 10 mM, KCl 60 mM, EDTA 1 mM, NP40 0.1%, DTT 1mM, sucrose, 0.34 M) and lysed with TRIzol.
648 Total RNA was purified by phenol–chloroform extraction and then treated with DNase I (Thermo) for
649 15min at 37 °C. Biotinylation of 4sU-labeled RNA was performed using EZ-Link Biotin-HPDP (Thermo
650 Fisher Scientific) at room temperature in the dark. Biotinylated samples were extracted using VAHTS
651 RNA clean beads (Vazyme) to remove free biotin-XX, and biotinylated RNA was captured using MyOne
652 C1 streptavidin-coupled beads (Thermo Fisher Scientific). After washing, the biotinylated RNA was
653 eluted with DTT. The eluted RNA was precipitated and subjected to reverse transcription and
654 quantitative PCR. The primers used for the TT-qPCR are listed in Supplementary Table 5.

655

656 **Dot blot**

657 For m^1A detection, caRNA was extracted and quantified using a nanodrop spectrophotometer. RNA
658 was then cross-linked to a nylon membrane and positively charged (Sigma) via UV irradiation. The
659 membrane was blocked with 5% nonfat dry milk in 1× TBST for 1 h at RT, followed by overnight
660 incubation at 4 °C with m^1A antibody. After incubation with the primary antibody, HRP-conjugated
661 secondary antibodies were applied for 1 h at room temperature. The signal was visualized using
662 Clarity Western ECL Substrate (Bio-Rad). After signal detection, the membrane was stained with
663 methylene blue, and images were captured.

664

665 **Immunoblotting**

666 Whole-cell extracts were prepared using RIPA buffer (50 mM Tris pH 7.4, 150 mM NaCl, 1% NP-40,
667 0.5% sodium deoxycholate, 0.1% SDS) containing protease inhibitor cocktail. For immunoblotting, 30-
668 50 μg of proteins was subjected to SDS-PAGE and transferred to polyvinylidene difluoride membranes
669 (PVDF, Bio-Rad). Blots were first blocked with 5% fat-free milk, then incubated with primary
670 antibodies and appropriate horseradish peroxidase conjugated secondary antibodies. Protein signals
671 were detected using Clarity Western ECL Substrate.

672

673 For fractionation, cells were treated as indicated, washed with Tris-buffered saline containing
674 protease and phosphatase inhibitor cocktails (Sigma–Aldrich), and harvested by centrifugation (300
675 g; 20 min; 4 °C). Lysis was carried out in sucrose buffer I (10 mM HEPES pH 7.9, 0.34 M sucrose, 3 mM
676 $CaCl_2$, 2 mM magnesium acetate, 0.1 mM EDTA, and 0.5% NP-40) for 20 min at 4 °C with rotation.
677 Nuclei were pelleted (3,900 g; 20 min; 4 °C) and washed once with sucrose buffer I without NP-40.
678 Lysis of Nuclei were carried out in nucleoplasm lysis buffer (20 mM HEPES pH 7.9, 3 mM EDTA, 10%
679 glycerol, 150 mM potassium acetate and 1.5 mM $MgCl_2$) by performing 20 strokes with a dounce
680 homogenizer on ice. Lysed nuclei were incubated for 30 min on ice and homogenized for 30 strokes.
681 Benzonase (25 units; Merck) was added and incubated for 1 h at 16 °C. Insolubilized chromatin was
682 pelleted by centrifugation (18,000 g, 30 min, 4 °C), resuspended in Laemmli buffer containing
683 benzonase (five units) to release chromatin-bound proteins, incubated at room temperature for 1 h,
684 and heated for 15 min at 95 °C.

685

686 **Quantitative RT-PCR**

687 Total RNA was isolated from GSC under the indicated treatment conditions. Complementary DNA
688 (cDNA) was synthesized from 1 µg of total RNA using a High-Capacity cDNA Reverse Transcription Kit
689 (Thermo Fisher). Quantitative PCR was performed using SYBR Green Master Mix (Thermo Fisher
690 Scientific) on a CFX Connect Real-Time PCR System (Bio-Rad). The primer sequences used for qPCR
691 are listed in Supplementary Table 5.

692

693 **Protein mass spectrometry**

694 Biotinylated RNA and biotinylated m^1A-bearing RNA oligonucleotides were synthesized using
695 GeneLink and the sequences are listed in Supplementary Table S5. For RNA pull-down assays, 2 µg
696 RNA oligonucleotides were incubated with streptavidin beads at room temperature for 30 min. GSC
697 nuclei were isolated using sucrose buffer I as previously described. The nuclear fraction was lysed in
698 Pierce IP Lysis Buffer (Thermo Fisher Scientific), and cleared nuclear lysates were collected after
699 centrifugation at 12,000 rpm. A total of 2 µg of nuclear protein lysate was incubated with RNA–
700 streptavidin bead complexes at 4 °C for 3 h. Beads were washed three times with IP lysis buffer, and

bound proteins were processed for western blotting or mass spectrometry.

For mass spectrometry, bound proteins were eluted in 5% SDS buffer and digested using the S-Trap trypsin digestion method. Peptides were extracted with 70% acetonitrile/5% formic acid, vacuum dried, and reconstituted in 3% acetonitrile/0.1% formic acid. LC-MS/MS was performed using a nanoElute 2 UHPLC system coupled to a timsTOF Pro 2 mass spectrometer with a CaptiveSpray nanoelectrospray source. Approximately 200 ng of peptides was loaded onto an IonOpticks Aurora Gen3 C18 column and separated using a 60 min 2–35% acetonitrile gradient at 300 nL/min. The timsTOF Pro 2 was operated in the data-dependent PASEF mode over a scan range of 100–1700 m/z. Raw files were processed using MSFragger v3.6 and searched against the OpenProt RNA transcriptome database containing alternative protein sequences derived from Ensembl and NCBI RefSeq transcripts. Searches allowed a 10 ppm precursor mass tolerance of 20 ppm fragment mass tolerance, and up to two missed cleavage events. The false discovery rate was capped before exporting the raw peak areas. Differential binding analysis was performed in R using the DEP package based on the protein intensity. Differentially enriched proteins and peptide intensities are listed in Supplementary Table 3.

Lactate secretion assay

Lactate secretion was quantified using the Lactate Glo Assay (Promega). The GSCs were transduced with control shRNA or shRNAs targeting TRMT6 and TRMT61A. Following transduction, ten thousand cells were seeded in 12-well plates and cultured for 48 h. The culture supernatant was collected for analysis according to the manufacturer's instructions. The luminescence signals were detected using a microplate reader. A standard curve was generated using the lactate standards included in the kit to calculate the absolute concentration of lactate in the culture medium.

Glucose uptake assay

Glucose uptake was evaluated using the Glucose Uptake Glo Assay (Promega). The GSCs were

transduced with lentiviral vectors expressing control shRNAs or shRNAs targeting TRMT6 and TRMT61A. Following cell counting, 3,000 cells were seeded into 96 well plates and cultured for 12 h. The growth medium was removed and replaced with phosphate buffered saline. Uptake of the glucose analog was then initiated and detected by monitoring luciferase activity according to the standard protocol provided by the manufacturer. The luminescence signals were recorded using a microplate reader. The relative glucose uptake levels were calculated by normalizing the luminescence intensity to that of the control group.

Seahorse XF96 respirometry

Cells (5,000 cells per well) were seeded in an XF96 plate and stabilized overnight. The extracellular acidification rate (ECAR) was measured using an XF96 extracellular flux analyzer with a glycolysis stress test kit (Agilent). The ECAR measurements were performed according to the manufacturer's instructions. The results were analyzed using the Wave software (Seahorse/Agilent).

Virtual screening docking

Virtual screening and molecular docking were performed using Discovery Studio 3.5. The crystal structure of the human TRMT6/TRMT61A complex (PDB: 5CCB) was obtained from the Protein Data Bank. The protein structure was prepared by removing water molecules and alternating conformations, adding hydrogen atoms, and repairing incomplete amino acid residues. The FDA-approved drug library was downloaded from MedChemExpress (MCE) and docked into the SAM-binding pocket of TRMT61A. Initial virtual screening was performed using the LibDock module in Discovery Studio 3.5, which treats the receptor as rigid and docks ligands based on predefined binding site features. Docking scores are presented in Supplementary Table 4.

Cellular Thermal Shift Assay

Cellular thermal shift assay (CETSA) was performed using GSC387 cells that stably expressed Flag-TRMT61A. Approximately 1×10^7 cells were treated with 20 μM paliperidone for 6 h before thermal

challenge. Cells were collected, washed with ice-cold PBS, and resuspended in 1.5 mL of PBS supplemented with protease inhibitors. The cell suspension was divided into seven 100 µL aliquots in 0.2 mL PCR tubes. Each aliquot was heated to the indicated temperature for 3 min using a Bio-Rad T100 Thermal Cycler, followed by cooling at room temperature for 3 min. Cells were lysed by three freeze–thaw cycles using dry ice and a thermal cycler set at 25 °C. Insoluble proteins and cell debris were removed by centrifugation at 10,000 × g for 20 min at 4 °C. Soluble fractions were collected and analyzed by western blotting.

Surface Plasmon Resonance Assay

Surface plasmon resonance (SPR) was used to measure the binding of paliperidone to recombinant human TRMT61A (active motif). The human TRMT61A protein was immobilized on a CM5 sensor chip using standard amine-coupling chemistry. PBST was used as the immobilization buffer, and PBST containing 1% DMSO was used as the running and interaction buffers. For immobilization, the CM5 chip surface was activated with 1-ethyl-3-(3-dimethylaminopropyl) carbodiimide and N-hydroxysuccinimide, at a flow rate of 10 µL/min. Human TRMT61A protein was diluted to 50 µg/mL in sodium acetate buffer and coupled to Channel 4 at 10 µL/min. The remaining active esters were quenched with ethanolamine. A reference channel was processed in parallel using the same activation and blocking procedures but without protein immobilization. For binding analysis, paliperidone was serially diluted in interaction buffer containing 1% DMSO and injected over the TRMT61A-coupled surface from low to a concentration of 30 µL/min. Sensorgrams were reference-subtracted and analyzed using the Biacore Insight Evaluation Software. Binding kinetics were calculated by global fitting to a 1:1 Langmuir binding model.

DepMap pharmacogenomic analysis

DepMap gene expression data, PRISM Repurposing primary viability AUC data, and cell line annotation files were downloaded from the DepMap database. The core m^1A-regulated gene signature was used to calculate an m^1A signature score for each cell line by averaging the expression levels of signature genes present in the DepMap expression matrix. The m^1A signature scores were

then merged with the PRISM drug response data using DepMap cell-line identifiers. To identify drugs whose response was associated with m^1A signature activity, Spearman's correlation analysis was performed between the m^1A signature score and the AUC value of each drug across cell lines. Drugs with sufficient available measurements were included in the analysis, and P-values were adjusted for multiple comparisons using the Benjamini–Hochberg false discovery rate method. For glioma-specific analysis, glioma cell lines were selected based on lineage subtype annotation and the same correlation analysis was performed within this subset.

Cell Proliferation and Extreme Limiting Dilution Assays

Cell proliferation was assessed by directly counting the number of cells. Cells were seeded onto plates and counted on days 0, 3, and 5. To evaluate neurosphere formation capacity, *in vitro* extreme limiting dilution assays were performed. Cells were plated at decreasing densities (100, 50, 20, 10, 5, and 2 cells/well) into 96-well plates. The presence and number of neurospheres in each well were recorded 7–14 d after plating. Data were analyzed using the software available at http://bioinf.wehi.edu.au/software/elda.

Public GSC datasets and glioma patient database

H3K27ac ChIP-seq, H3K4me3 ChIP-seq, and ATAC-seq data for GSCs are available in prior publications[7,9,56,96]. Glioma samples from CGGA and TCGA were retrieved using GlioVis (http://gliovis.bioinfo.cnio.es) and GEPIA2 (http://gepia2.cancer-pku.cn/)[97,98]. Survival analysis for the m^1A signature was performed using Kaplan–Meier curves and log-rank tests in R. Single-cell analysis of TRMT6 and TRMT61A mRNA expression was performed using the GSE131928 dataset through the Broad Institute Single Cell Portal[1]. Genome-wide screens analyzed using the BAGEL algorithm and Screens from the DepMap project analyzed by Chronos were used to investigate the dependencies of RNA modification regulators in GSC. For comparison between GSC screens, NSC screens, and GBM cell lines, quantile normalization was performed on the BF scores. Differences in average quantile normalized BF scores between GSC, NSC, and GBM screens are presented in a scatter plot.

Statistical analysis

All statistical analyses are described in the figure legends. Statistical tests, including two-tailed unpaired t-test, one-way ANOVA, two-way ANOVA, and log-rank test, were performed using R or Prism 9 software. Unless otherwise indicated, data in the figures are presented as mean ± SD. In the box-and-whisker plot, boxes represent data within the 25th to 75th percentiles, whiskers depict the range of all data points, and horizontal lines within boxes represent mean values.

Data availability

Raw and processed sequencing data for caRNA-seq, RNA-seq, RIP-seq, and ChIP-seq were deposited in Gene Expression Omnibus (GEO: https://www.ncbi.nlm.nih.gov/geo/). Reviewer access tokens are as follows: caRNA-seq (GSE316201; cdkbicgqfzylxol), RNA-seq (GSE316202; crevqwqednsjrcr), RIP-seq (GSE316204; udgnywaovvsjhox), and ChIP-seq (GSE316207; grwleuimntwzxav). The mass spectrometry proteomics data were deposited in the ProteomeXchange Consortium via the PRIDE[99] partner repository with the dataset identifier PXD080795. All other data supporting the findings of this study are available from the corresponding author upon request.

Code availability

No custom code was generated for this study.

Materials & Correspondence

Correspondence and requests for materials should be addressed to J.N.R.

ACKNOWLEDGEMENTS

We thank the Microscopy Facility of the Dietrich School of Arts and Sciences at the University of Pittsburgh for assistance with immunofluorescence analysis, and the Mass Spectrometry Laboratory of the School of Chemical Sciences at the University of Illinois Urbana-Champaign for LC-MS/MS analysis. This work was supported by NIH grants (R35CA197718, R01CA238662, R01CA268634, and R01NS103434 to J.N.R.), the Defense Health Agency (HT9425-23-1-0689 to J.N.R.), the American Cancer Society Lisa Dean Mosley Cancer Stem Cell Consortium (CSCC-LEAD-22-186-01-CSCC to J.N.R.), and start-up funds from the University of Pittsburgh (to J.N.R.).

AUTHOR CONTRIBUTIONS

D.W. and J.N.R. conceived of the project, designed the experiments, and wrote the manuscript. D.W. performed most of the experiments and analyzed the data. S.T. helped edit the manuscript. W. W., Q. W., T. H., D. L., P. Z., F. Y., R. W., H. L., Z. C., H. M., and T. D. contributed to cell culture and mouse experiments. C.S., Z.Z., and X.M. performed LC–MS/MS analyses. H.Y., X.W., Y.H., J.Z., and C.H. provided scientific advice and critical input.

DECLARATION OF INTERESTS

The authors declare no competing interests.

SUPPLEMENTARY TABLES

Table S1. Differential analysis of RNA modifications in caRNA detected by LC–MS/MS.

Table S2. Comparative qBF scores of RNA modification regulators across published datasets.

Table S3. Differential protein enrichment analysis from RNA pull-down mass spectrometry.

Table S4. Docking scores from virtual screening of the FDA-approved drug library.

Table S5. Primers and shRNAs used in this study.

Figure 1

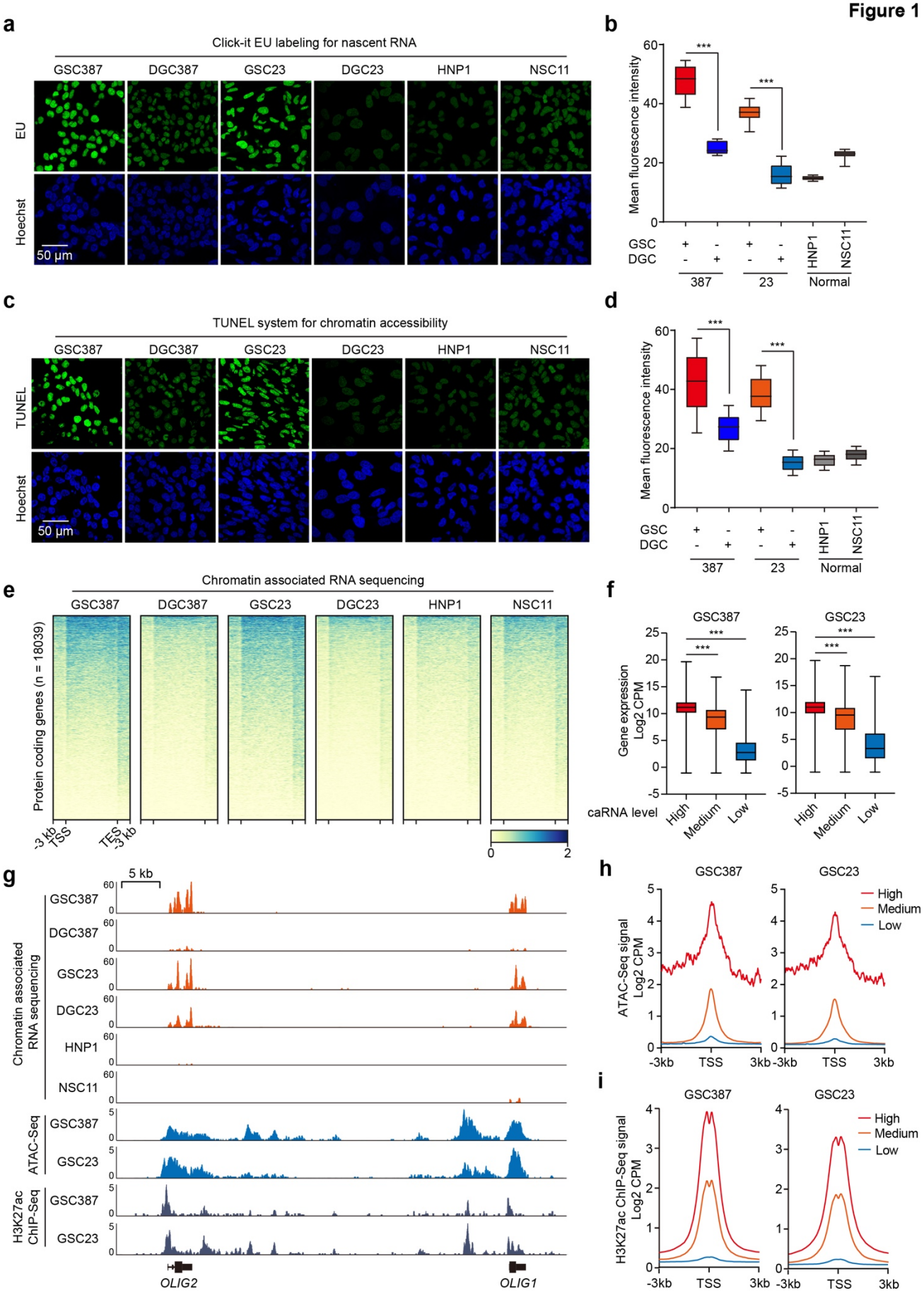
a
Click-it EU labeling for nascent RNA
GSC387
DGC387
GSC23
DGC23
HNP1
NSC11
EU
Hoechst
50 μm
b
Mean fluorescence intensity
***
***
GSC
DGC
387
23
Normal
HNP1
NSC11
c
TUNEL system for chromatin accessibility
TUNEL
d
e
Chromatin associated RNA sequencing
Protein coding genes (n = 18039)
TSS
TES
f
GSC387
GSC23
Gene expression Log2 CPM
caRNA level
High
Medium
Low
g
5 kb
Chromatin associated RNA sequencing
ATAC-Seq
H3K27ac ChIP-Seq
OLIG2
OLIG1
h
ATAC-Seq signal Log2 CPM
i
H3K27ac ChIP-Seq signal Log2 CPM

Figure Legends

Fig. 1 Hyperactive chromatin landscape and caRNA accumulation in glioma stem cells.

(a and b) Representative images (A) and quantification (B) of nascent RNA synthesis in GSCs, DGCs, and NSCs. Cells were incubated with EU for 30 minutes followed by labeling via click chemistry. Scale bars represent 50 µm. Data in (B) are presented as mean fluorescence intensity ± SD (n = 10). EU, 5-ethynyl uridine. *P* values were calculated by the Wilcoxon test. ***p < 0.001.

(c and d) Assessment of chromatin accessibility using DNase I digestion coupled with TUNEL labeling. Representative images (C) and quantification (D) in GSCs, DGCs, and NSCs are shown. Scale bars represent 50 µm. Mean fluorescence intensity in (D) is presented as mean ± SD (n = 10). *P* values were calculated by the Wilcoxon test. ***p < 0.001.

(e) Heatmap profiling of all genes encoding proteins comparing caRNA abundance across GSCs, DGCs, and NSCs.

(f) Genome browser tracks displaying caRNA signals, ATAC-Seq, and H3K27ac enrichment at the *OLIG1* and *OLIG2* loci.

(g) Box plots of gene expression from RNA-Seq in GSC387 and GSC23 stratified by genes with high, medium, and low caRNA abundance.

(h) Metagene plots of ATAC sequencing signals centered on the transcription start site in GSC387 and GSC23 stratified by caRNA levels.

(i) Metagene plots of H3K27ac signals centered on the transcription start site in GSC387 and GSC23 stratified by caRNA levels.

Figure 2

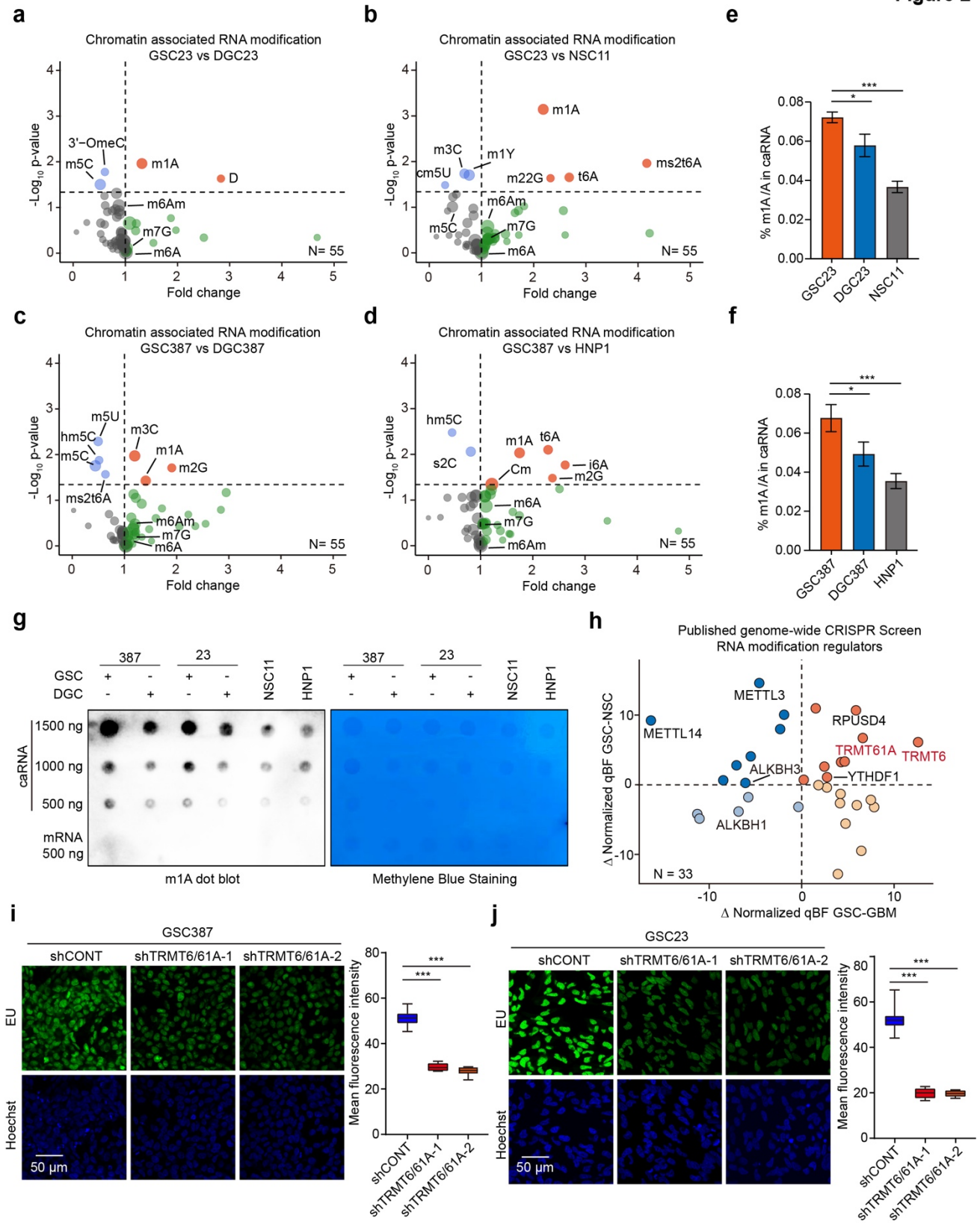
a
Chromatin associated RNA modification
GSC23 vs DGC23
-Log10 p-value
Fold change
3'-OmeC
m5C
m1A
D
m6Am
m7G
m6A
N= 55
b
Chromatin associated RNA modification
GSC23 vs NSC11
m1A
m3C
m1Y
cm5U
m22G
t6A
ms2t6A
m6Am
m5C
m7G
m6A
N= 55
e
% m1A /A in caRNA
GSC23
DGC23
NSC11
c
Chromatin associated RNA modification
GSC387 vs DGC387
m5U
hm5C
m5C
m3C
m1A
m2G
ms2t6A
m6Am
m7G
m6A
N= 55
d
Chromatin associated RNA modification
GSC387 vs HNP1
hm5C
s2C
m1A
t6A
Cm
i6A
m2G
m6A
m7G
m6Am
N= 55
f
% m1A /A in caRNA
GSC387
DGC387
HNP1
g
387
23
GSC
DGC
NSC11
HNP1
caRNA
1500 ng
1000 ng
500 ng
mRNA
500 ng
m1A dot blot
Methylene Blue Staining
h
Published genome-wide CRISPR Screen
RNA modification regulators
METTL3
METTL14
RPUSD4
TRMT61A
TRMT6
ALKBH3
YTHDF1
ALKBH1
N = 33
Δ Normalized qBF GSC-NSC
Δ Normalized qBF GSC-GBM
i
GSC387
shCONT
shTRMT6/61A-1
shTRMT6/61A-2
EU
Hoechst
50 μm
Mean fluorescence intensity
j
GSC23
shCONT
shTRMT6/61A-1
shTRMT6/61A-2
EU
Hoechst
50 μm
Mean fluorescence intensity

880

Fig. 2 Elevated m^1A deposition on chromatin-associated RNAs in glioma stem cells.

(a and b) Volcano plots showing differential abundance of 55 RNA modifications detected by LC–MS/MS in caRNAs purified from GSC23, DGC23, and NSC11. (A) GSC23 versus DGC23. (B) GSC23 versus NSC11.

(c and d) Volcano plots showing differential abundance of RNA modifications in caRNAs purified from GSC387, DGC387, and HNP1. (C) GSC387 versus DGC387. (D) GSC387 versus HNP1.

(e) Quantification of the m^1A/A ratio in caRNAs isolated from GSC23, DGC23, and NSC11. One-way ANOVA with Bonferroni correction was used. *$p < 0.05$, ***$p < 0.001$.

(f) Quantification of the m^1A/A ratio in caRNAs isolated from GSC387, DGC387, and HNP1. One-way ANOVA with Bonferroni correction was used. *$p < 0.05$, ***$p < 0.001$.

(g) Dot blot validation of elevated m^1A levels in caRNAs and mRNA from GSCs, DGCs, and NSCs. Methylene blue staining was used as a loading control.

(h) Scatterplot of RNA modification genes using normalized quantitative Bayes factor (qBF) scoring from genome-wide CRISPR screens. The x-axis indicates the mean qBF in GSC lines minus GBM cell lines and the y-axis indicate the mean qBF in GSC lines minus NSC cell lines.

(i and j) Representative images and quantification of nascent RNA synthesis following TRMT6/61A depletion in GSC23 (I) and GSC387 (J). Mean fluorescence intensity is shown as mean ± SD (n = 10). Statistical significance was assessed using the Wilcoxon test. ***$p < 0.001$.

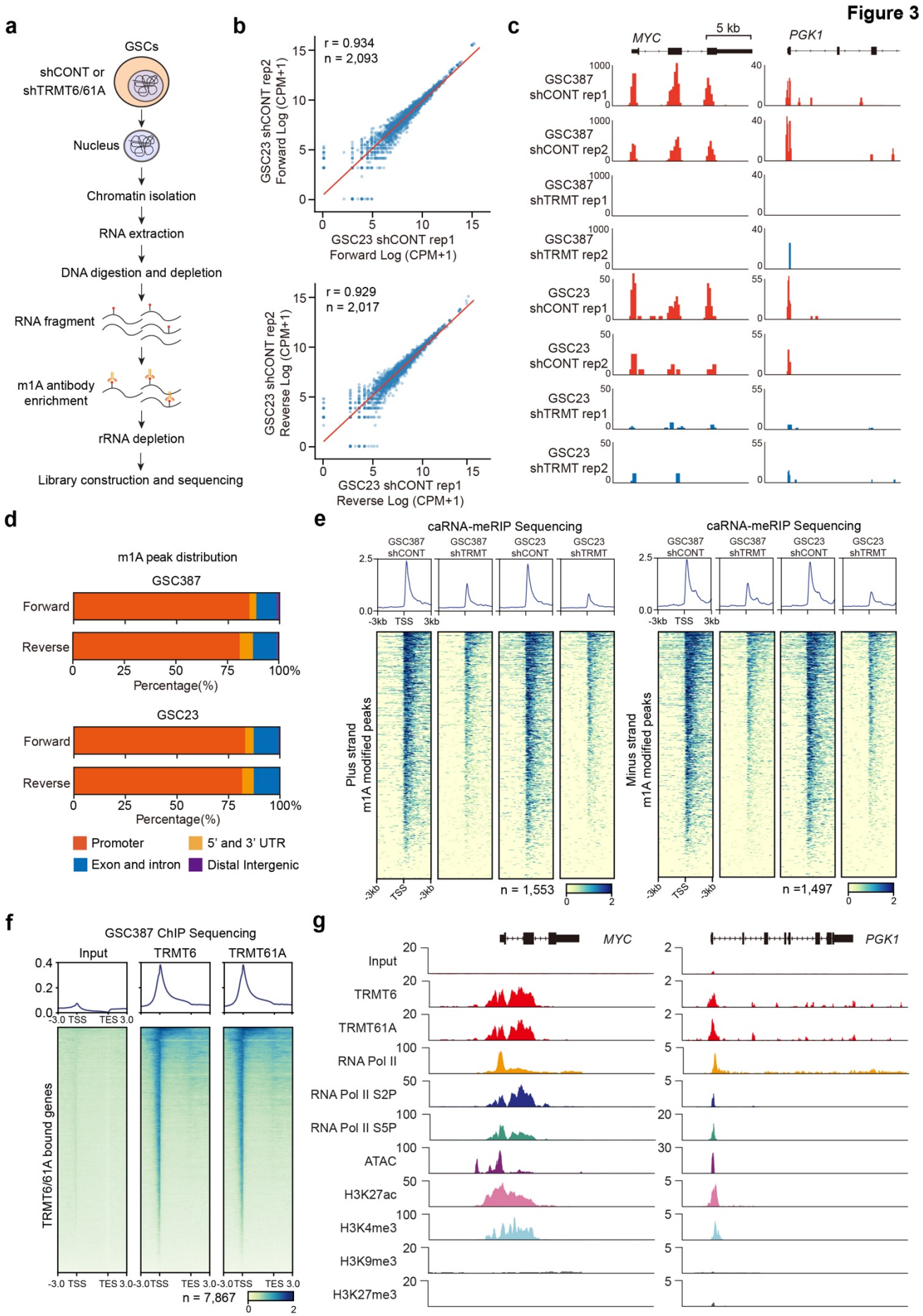
Figure 3
a
GSCs
shCONT or shTRMT6/61A
Nucleus
Chromatin isolation
RNA extraction
DNA digestion and depletion
RNA fragment
m1A antibody enrichment
rRNA depletion
Library construction and sequencing
b
r = 0.934
n = 2,093
GSC23 shCONT rep2 Forward Log (CPM+1)
GSC23 shCONT rep1 Forward Log (CPM+1)
r = 0.929
n = 2,017
GSC23 shCONT rep2 Reverse Log (CPM+1)
GSC23 shCONT rep1 Reverse Log (CPM+1)
c
MYC
5 kb
PGK1
GSC387 shCONT rep1
GSC387 shCONT rep2
GSC387 shTRMT rep1
GSC387 shTRMT rep2
GSC23 shCONT rep1
GSC23 shCONT rep2
GSC23 shTRMT rep1
GSC23 shTRMT rep2
d
m1A peak distribution
GSC387
Forward
Reverse
Percentage(%)
GSC23
Promoter
5' and 3' UTR
Exon and intron
Distal Intergenic
e
caRNA-meRIP Sequencing
GSC387 shCONT
GSC387 shTRMT
GSC23 shCONT
GSC23 shTRMT
-3kb TSS 3kb
Plus strand m1A modified peaks
Minus strand m1A modified peaks
n = 1,553
n =1,497
f
GSC387 ChIP Sequencing
Input
TRMT6
TRMT61A
-3.0 TSS TES 3.0
TRMT6/61A bound genes
n = 7,867
g
MYC
PGK1
Input
TRMT6
TRMT61A
RNA Pol II
RNA Pol II S2P
RNA Pol II S5P
ATAC
H3K27ac
H3K4me3
H3K9me3
H3K27me3

Fig. 3 caRNA m^1A enriched at TSS sites.

(a) Schematic workflow illustrating the enrichment of caRNAs modified by m^1A. Nuclei were isolated from control GSCs or cells depleted of TRMT6 and TRMT61A. Following nuclear RNA extraction and digestion with DNase I, immunoprecipitation was performed utilizing an antibody specific for m^1A. Modified transcripts were subsequently captured using Protein A/G beads and subjected to rRNA depletion prior to library preparation for sequencing.

(b) Correlation analysis between two biologically independent GSC23 replicates, with each dot representing an individual peak quantified by CPM (counts per million).

(c) Representative genome browser tracks illustrating m^1A peak distribution on *MYC* and *PGK1* caRNAs under the indicated conditions.

(d) Genome distribution of m^1A peaks on caRNAs in GSC387 and GSC23 across both forward and reserve strands.

(e) Metagene profiles and heatmaps showing the distribution of sense (left) and antisense (right) m^1A signals around transcription start sites of caRNA-associated genes.

(f) Heatmap of ChIP sequencing data displaying the occupancy of TRMT6 and TRMT61A at transcription start sites of genes encoding proteins.

(g) Genome browser tracks illustrating co-occupancy of TRMT6 and TRMT61A with RNA Polymerase II and histone marks at the *MYC* and *PGK1* loci. Public datasets for ATAC sequencing and ChIP sequencing of H3K27ac and H3K4me3 as well as repressive marks H3K9me3 and H3K27me3 in GSC387 were utilized for comparison.

Figure 4

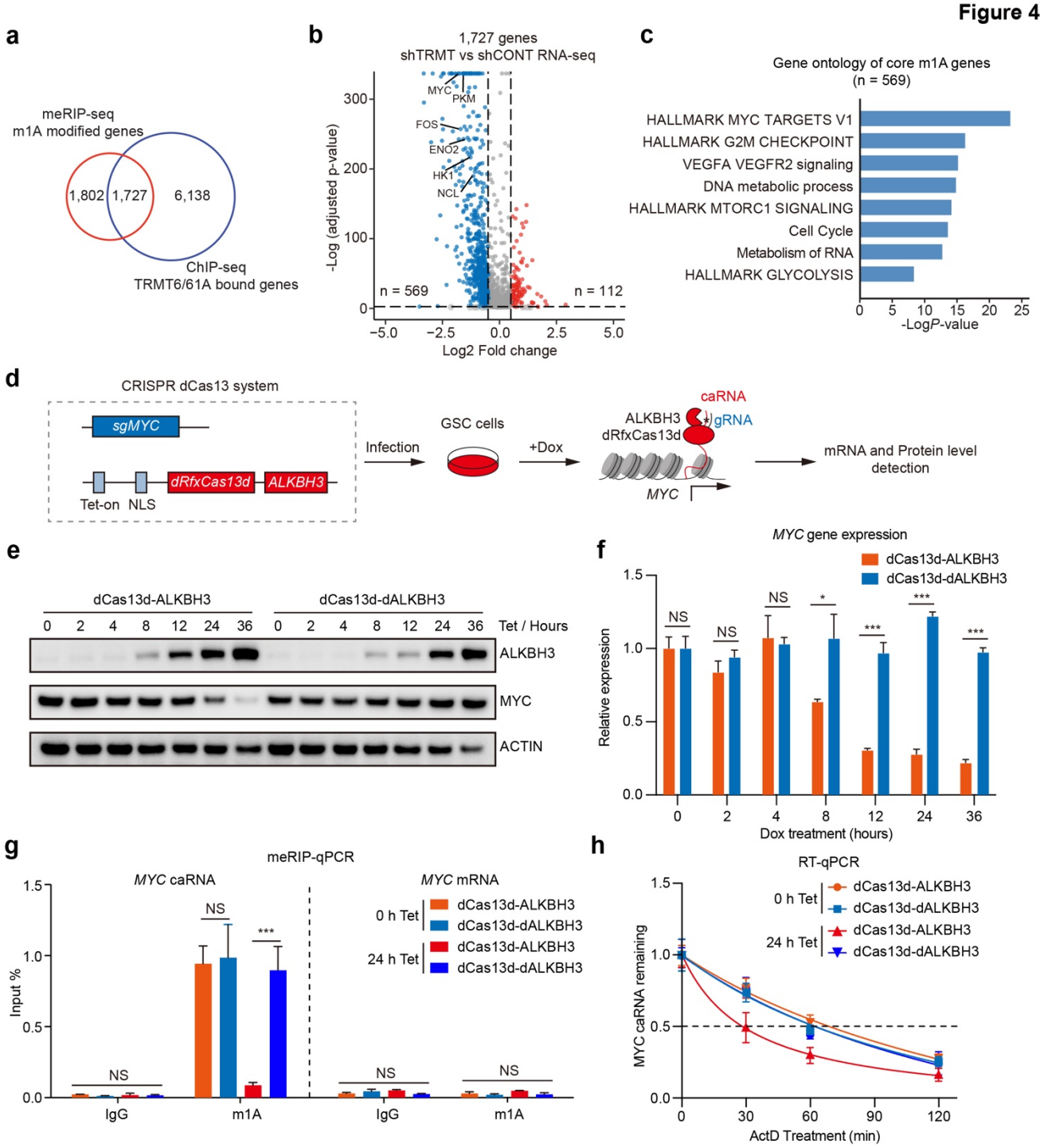
a
meRIP-seq
m1A modified genes
1,802
1,727
6,138
ChIP-seq
TRMT6/61A bound genes
b
1,727 genes
shTRMT vs shCONT RNA-seq
MYC
PKM
FOS
ENO2
HK1
NCL
-Log (adjusted p-value)
n = 569
n = 112
Log2 Fold change
c
Gene ontology of core m1A genes
(n = 569)
HALLMARK MYC TARGETS V1
HALLMARK G2M CHECKPOINT
VEGFA VEGFR2 signaling
DNA metabolic process
HALLMARK MTORC1 SIGNALING
Cell Cycle
Metabolism of RNA
HALLMARK GLYCOLYSIS
-LogP-value
d
CRISPR dCas13 system
sgMYC
Tet-on
NLS
dRfxCas13d
ALKBH3
Infection
GSC cells
+Dox
caRNA
ALKBH3
dRfxCas13d
gRNA
MYC
mRNA and Protein level
detection
e
dCas13d-ALKBH3
dCas13d-dALKBH3
Tet / Hours
ALKBH3
MYC
ACTIN
f
MYC gene expression
dCas13d-ALKBH3
dCas13d-dALKBH3
Relative expression
Dox treatment (hours)
g
meRIP-qPCR
MYC caRNA
MYC mRNA
0 h Tet
24 h Tet
dCas13d-ALKBH3
dCas13d-dALKBH3
Input %
IgG
m1A
h
RT-qPCR
MYC caRNA remaining
ActD Treatment (min)

Fig. 4 caRNA m^{1}A regulates MYC-driven transcription program.

(a) Venn diagram showing the overlap between m^{1}A-modified genes identified by m^{1}A RIP-seq and TRMT6/TRMT61A-bound genes identified by ChIP-seq in GSC387.

(b) Volcano plot showing differential expression of 1,727 genes marked by m^{1}A on their caRNAs following TRMT6/61A depletion. Upregulated genes are highlighted in red, and downregulated genes in blue.

(c) Bar graph showing Gene Ontology analysis of the core m^{1}A-regulated gene signature performed using Metascape.

(d) Schematic of the CRISPR–dCas13 system designed to remove m^{1}A from *MYC* promoter-associated caRNA. Two plasmids were engineered: an sgRNA-expressing vector targeting *MYC* caRNA, and a doxycycline-inducible dRfxCas13d-ALKBH3 (wild-type or catalytically inactive) fusion construct. Both plasmids were introduced into GSC387 cells for functional validation.

(e) Western blot showing doxycycline-induced expression of MYC protein and the dRfxCas13d–ALKBH3 fusion proteins over the indicated time course. Anti-ALKBH3 antibody was used to detect both WT and mutant fusion proteins. Actin used as the loading control.

(f) qPCR quantification of MYC mRNA levels at the indicated time points following doxycycline-induced activation of the CRISPR–dCas13-based m^{1}A removal system.

(g) MeRIP-qPCR analysis showing m^{1}A enrichment on MYC caRNA at the indicated time points after doxycycline-induced activation of the CRISPR–dCas13-based m^{1}A removal system. Mature MYC mRNA was included as a control.

(h) Following doxycycline treatment, cells were treated with actinomycin D (ActD), and remaining MYC caRNA levels were measured at the indicated time points to assess caRNA stability. One-way ANOVA with Bonferroni correction was used. *$p < 0.05$, ***$p < 0.001$.

Figure 5

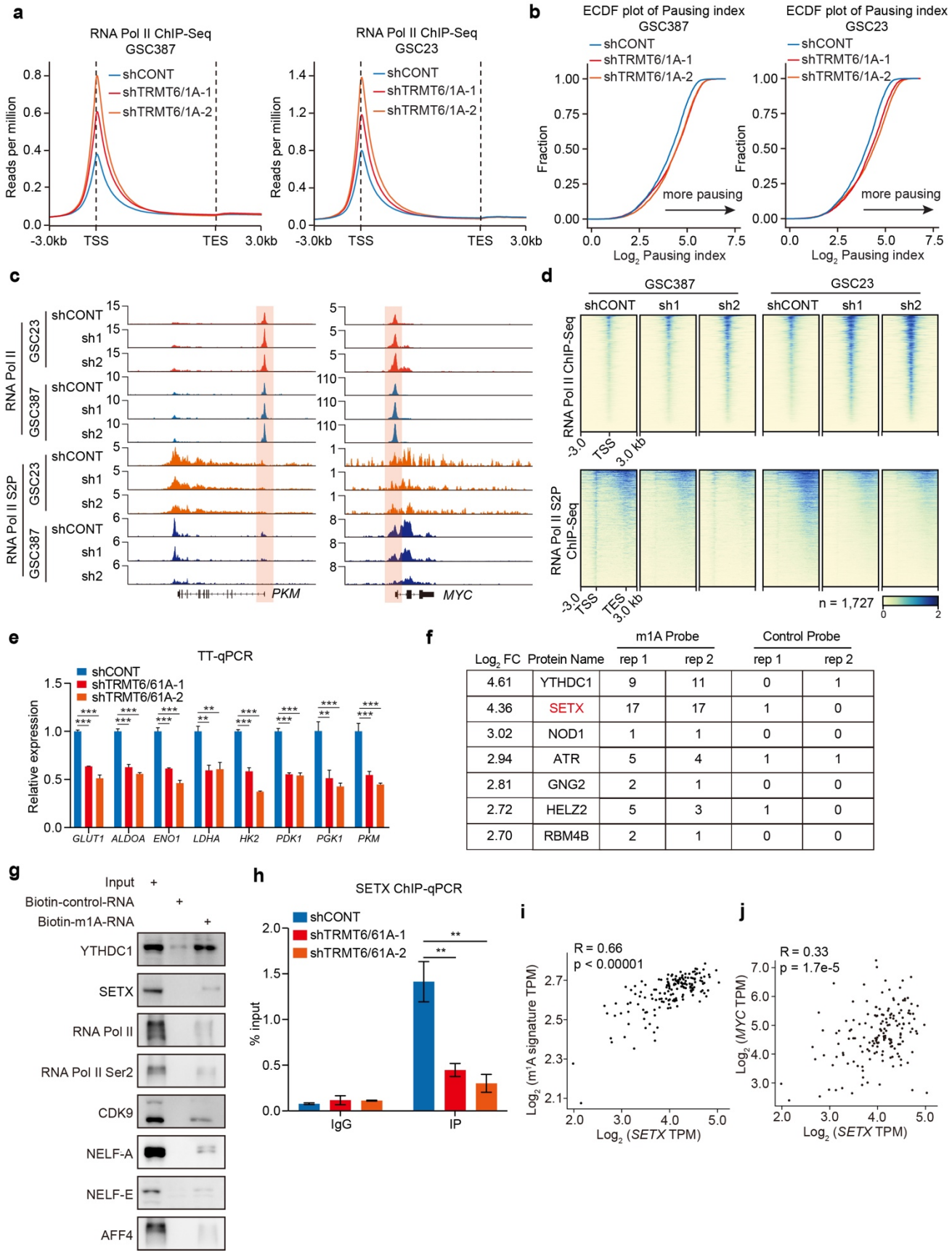
a
RNA Pol II ChIP-Seq
GSC387
RNA Pol II ChIP-Seq
GSC23
shCONT
shTRMT6/1A-1
shTRMT6/1A-2
Reads per million
-3.0kb
TSS
TES
3.0kb
b
ECDF plot of Pausing index
GSC387
ECDF plot of Pausing index
GSC23
Fraction
more pausing
Log2 Pausing index
c
RNA Pol II
RNA Pol II S2P
GSC23
GSC387
shCONT
sh1
sh2
PKM
MYC
d
GSC387
GSC23
shCONT
sh1
sh2
RNA Pol II ChIP-Seq
RNA Pol II S2P ChIP-Seq
n = 1,727
e
TT-qPCR
shCONT
shTRMT6/61A-1
shTRMT6/61A-2
Relative expression
GLUT1
ALDOA
ENO1
LDHA
HK2
PDK1
PGK1
PKM
f
m1A Probe
Control Probe
Log2 FC
Protein Name
rep 1
rep 2
rep 1
rep 2
4.61 YTHDC1 9 11 0 1
4.36 SETX 17 17 1 0
3.02 NOD1 1 1 0 0
2.94 ATR 5 4 1 1
2.81 GNG2 2 1 0 0
2.72 HELZ2 5 3 1 0
2.70 RBM4B 2 1 0 0
g
Input
Biotin-control-RNA
Biotin-m1A-RNA
YTHDC1
SETX
RNA Pol II
RNA Pol II Ser2
CDK9
NELF-A
NELF-E
AFF4
h
SETX ChIP-qPCR
shCONT
shTRMT6/61A-1
shTRMT6/61A-2
% input
IgG
IP
i
R = 0.66
p < 0.00001
Log2 (m1A signature TPM)
Log2 (SETX TPM)
j
R = 0.33
p = 1.7e-5
Log2 (MYC TPM)
Log2 (SETX TPM)

Fig. 5 m^1A facilitates Pol II pause release and transcriptional elongation.

(a) Metagene profiles showing the distribution of RNA Polymerase II following depletion of TRMT6 and TRMT61A compared to the control conditions in GSC387 (left) and GSC23 (right).

(b) Empirical cumulative density function plots illustrating the RNA Polymerase II pausing index in control cells versus cells depleted of TRMT6 and TRMT61A.

(c) Representative genome tracks for *MYC* and *PKM* displaying ChIP sequencing signals for RNA Polymerase II and Ser2P at the promoter and gene body, respectively, under the indicated conditions.

(d) Heatmaps showing the density of RNA Polymerase II (top) and Ser2 phosphorylated RNA Polymerase II (bottom) centered on the promoter regions or gene bodies of genes modified by m^1A upon knockdown of the TRMT6 and TRMT61A complex in GSC387 and GSC23.

(e) Quantification of nascent transcripts for glycolytic genes using metabolic labeling with 4sU followed by qPCR.

(f) Mass spectrometry analysis of proteins pulled down by the m^1A-modified probe and control probe in GSC387, showing log_2 fold changes in protein intensity and the number of peptides detected in each group.

(g) western blotting validation of proteins pulled down by the m^1A-modified probe in GSC387.

(h) SETX ChIP-qPCR analysis shows SETX enrichment at the MYC promoter after TRMT6/TRMT61A knockdown.

(i-j) Scatter plots showing the correlation between SETX expression and the core m^1A-regulated gene signature (i) or MYC expression (j) in TCGA GBM samples analyzed using GEPIA2. Data are presented as the mean ± SD. *P* value were determined using one-way ANOVA with Bonferroni correction. **p < 0.01, ***p < 0.001.

Figure 6

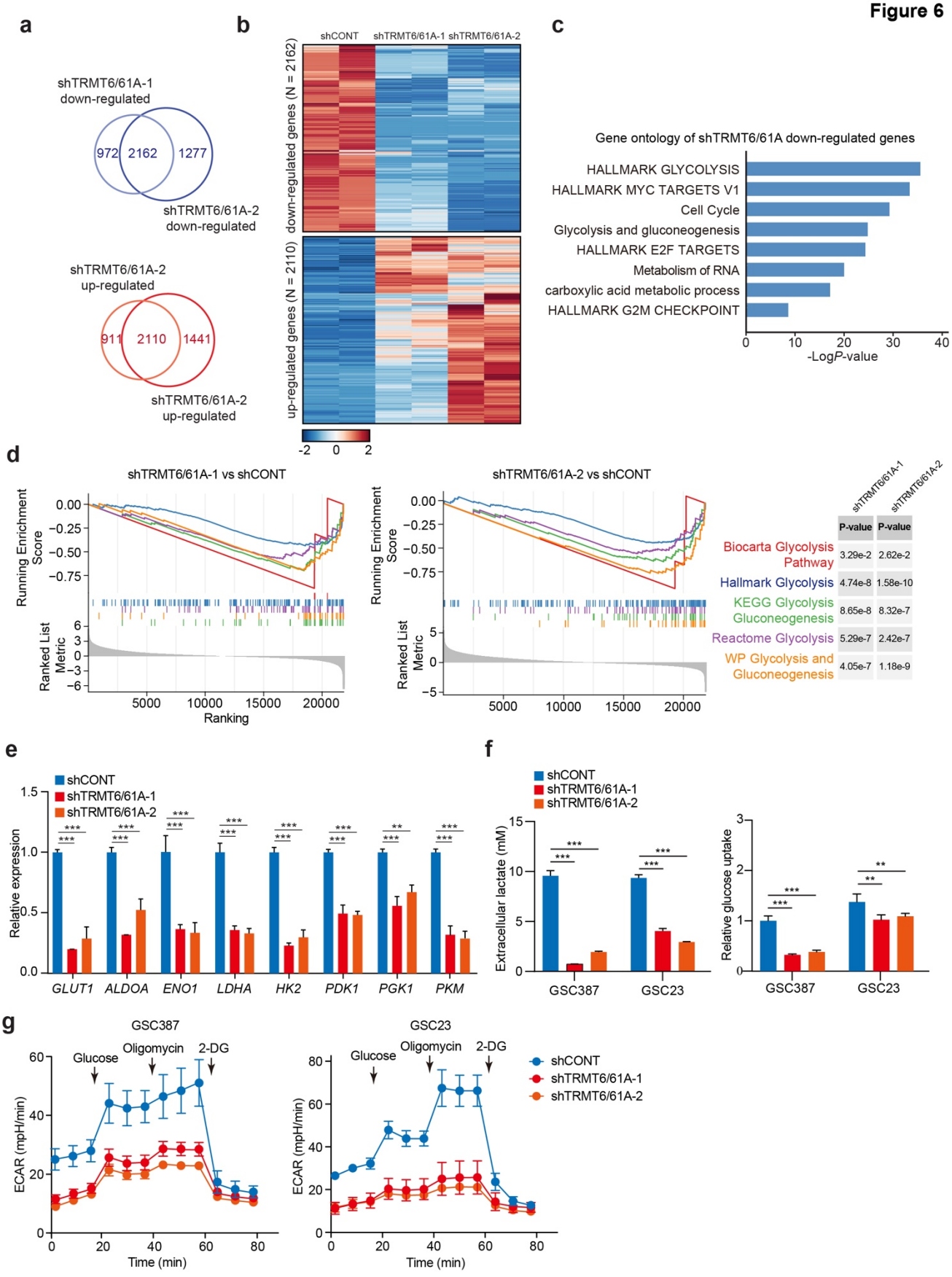
a
shTRMT6/61A-1
down-regulated
972
2162
1277
shTRMT6/61A-2
down-regulated
shTRMT6/61A-2
up-regulated
911
2110
1441
shTRMT6/61A-2
up-regulated
b
shCONT
shTRMT6/61A-1
shTRMT6/61A-2
down-regulated genes (N = 2162)
up-regulated genes (N = 2110)
-2
0
2
c
Gene ontology of shTRMT6/61A down-regulated genes
HALLMARK GLYCOLYSIS
HALLMARK MYC TARGETS V1
Cell Cycle
Glycolysis and gluconeogenesis
HALLMARK E2F TARGETS
Metabolism of RNA
carboxylic acid metabolic process
HALLMARK G2M CHECKPOINT
-LogP-value
d
shTRMT6/61A-1 vs shCONT
shTRMT6/61A-2 vs shCONT
Running Enrichment Score
Ranked List Metric
Ranking
shTRMT6/61A-1
shTRMT6/61A-2
P-value
P-value
Biocarta Glycolysis Pathway
3.29e-2
2.62e-2
Hallmark Glycolysis
4.74e-8
1.58e-10
KEGG Glycolysis Gluconeogenesis
8.65e-8
8.32e-7
Reactome Glycolysis
5.29e-7
2.42e-7
WP Glycolysis and Gluconeogenesis
4.05e-7
1.18e-9
e
shCONT
shTRMT6/61A-1
shTRMT6/61A-2
Relative expression
GLUT1
ALDOA
ENO1
LDHA
HK2
PDK1
PGK1
PKM
f
shCONT
shTRMT6/61A-1
shTRMT6/61A-2
Extracellular lactate (mM)
Relative glucose uptake
GSC387
GSC23
g
GSC387
GSC23
Glucose
Oligomycin
2-DG
ECAR (mpH/min)
Time (min)
shCONT
shTRMT6/61A-1
shTRMT6/61A-2

Fig.6 TRMT6 and TRMT61A regulate glycolytic programs.

(a) Venn diagrams showing the overlap of differentially expressed genes identified by two independent shRNA constructs targeting both TRMT6 and TRMT61A.

(b) Heatmap profiling the expression of genes upregulated and downregulated following depletion of TRMT6 and TRMT61A in GSC387 cells.

(c) Gene Ontology analysis of the downregulated gene set. The top enriched pathways are displayed.

(d) Gene Set Enrichment Analysis plots for five distinct glycolysis signatures. *P* values were calculated using the permutation test within the GSEA software.

(e) Validation of representative glycolytic genes using qPCR. Data are presented as mean ± SD. *P* value was determined using one-way ANOVA with Bonferroni correction. **p < 0.01, ***p < 0.001.

(f) Functional metabolic assays measuring lactate secretion and glucose uptake. Lactate levels in the culture medium were assessed 48 hours after transduction with control or shRNAs targeting TRMT6 and TRMT61A. Glucose uptake was measured utilizing 3,000 infected cells per assay. Data represent mean ± SD. *P* value was determined using one-way ANOVA with Bonferroni correction. **p < 0.01, ***p < 0.001.

(g) Glycolytic stress tests performed on a Seahorse XF bioanalyzer to determine the glycolytic capacity of control and knockdown cells. Cells were seeded at a density of 5,000 per well in XF96 plates (n = 5).

Figure 7

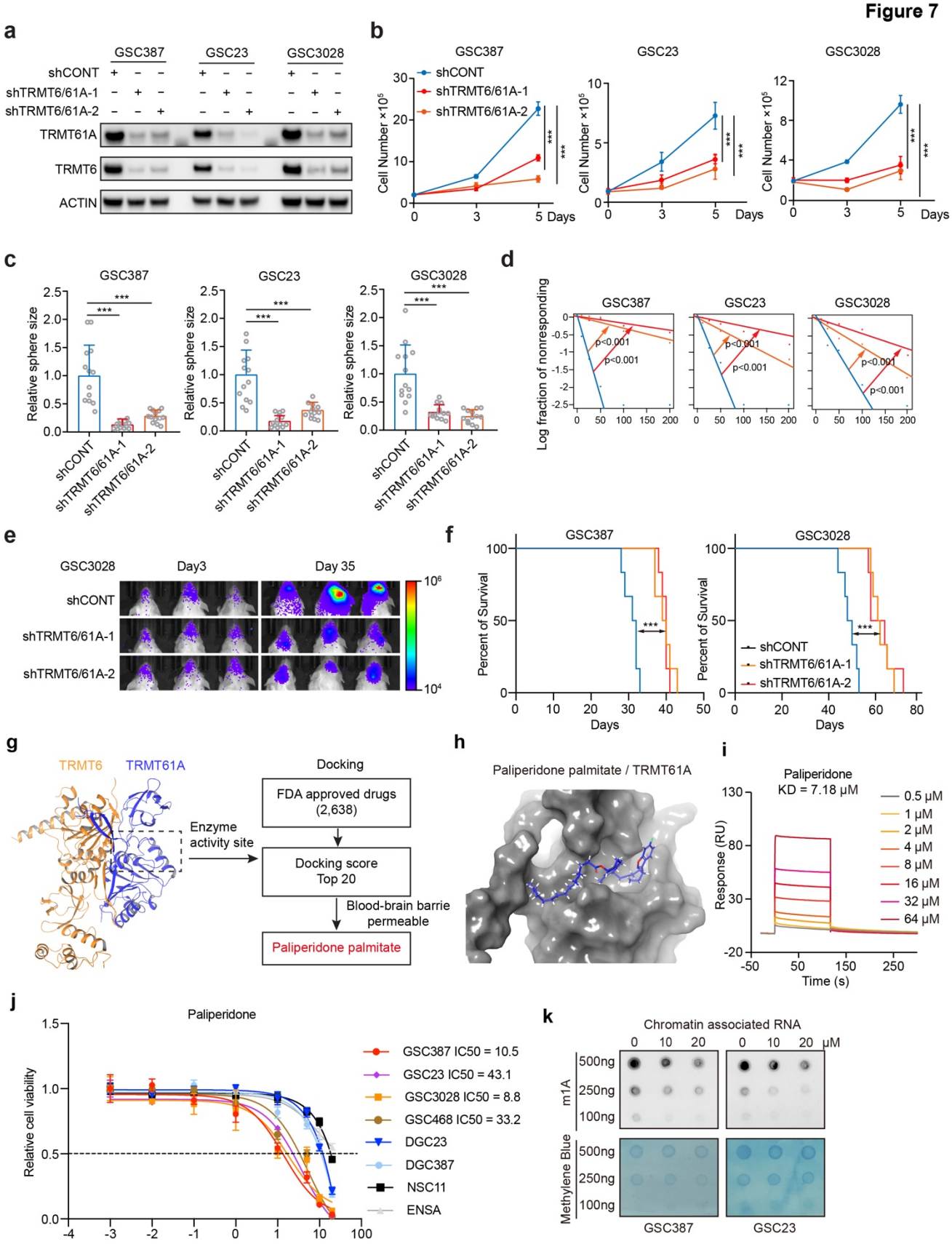
a
GSC387
GSC23
GSC3028
shCONT
shTRMT6/61A-1
shTRMT6/61A-2
TRMT61A
TRMT6
ACTIN
b
GSC387
GSC23
GSC3028
shCONT
shTRMT6/61A-1
shTRMT6/61A-2
Cell Number ×10^5
Days
c
GSC387
GSC23
GSC3028
Relative sphere size
shCONT
shTRMT6/61A-1
shTRMT6/61A-2
d
GSC387
GSC23
GSC3028
Log fraction of nonresponding
p<0.001
e
GSC3028
Day3
Day 35
shCONT
shTRMT6/61A-1
shTRMT6/61A-2
f
GSC387
GSC3028
Percent of Survival
Days
shCONT
shTRMT6/61A-1
shTRMT6/61A-2
g
TRMT6
TRMT61A
Enzyme activity site
Docking
FDA approved drugs (2,638)
Docking score Top 20
Blood-brain barrie permeable
Paliperidone palmitate
h
Paliperidone palmitate / TRMT61A
i
Paliperidone
KD = 7.18 μM
Response (RU)
Time (s)
0.5 μM
1 μM
2 μM
4 μM
8 μM
16 μM
32 μM
64 μM
j
Paliperidone
Relative cell viability
Log10 Paliperidone (μM)
GSC387 IC50 = 10.5
GSC23 IC50 = 43.1
GSC3028 IC50 = 8.8
GSC468 IC50 = 33.2
DGC23
DGC387
NSC11
ENSA
k
Chromatin associated RNA
0 10 20 0 10 20 μM
m1A
500ng
250ng
100ng
Methylene Blue
GSC387
GSC23

Fig. 7 Inhibition of TRMT6/61A attenuates GSC maintenance and GBM progression.

(a) Immunoblot verifying stable knockdown efficiency in three patient-derived GSC lines.

(b) Cell proliferation assays showing impaired growth rates in GSCs depleted of TRMT6 and TRMT61A. Data represent mean ± SD. Statistical significance was determined using two-way ANOVA with Bonferroni correction. ***p < 0.001.

(c) Quantification of sphere formation capacity in GSC387, GSC23, and GSC3028 expressing control or shRNAs targeting the writer complex. Data represent mean ± SD (n = 13 spheres per group). *P* values were calculated using one-way ANOVA with Bonferroni correction. ***p < 0.001.

(d) Extreme limiting dilution assays were performed to assess stem cell frequency in GSC387, GSC23, and GSC3028 following knockdown. *P* values were calculated using Extreme Limiting Dilution Analysis (ELDA) with a two-tailed likelihood-ratio test. ***p < 0.001.

(e) Representative bioluminescence imaging of mice bearing GSC3028 xenografts at day 3 and day 35 post implantation.

(f) Kaplan Meier survival curves of mice implanted with GSC387 and GSC3028 transduced with control or shRNAs targeting TRMT6 and TRMT61A (n = 6 mice per group). *P* values were determined using the log-rank test. ***p < 0.001.

(g) Structure-guided virtual docking of FDA-approved drugs against the catalytic pocket of TRMT61A based on the crystal structure of the TRMT6–TRMT61A complex.

(h) Predicted binding mode of paliperidone palmitate within the TRMT61A catalytic pocket.

(i) Surface plasmon resonance (SPR) analysis measuring the binding affinity between recombinant TRMT61A protein and paliperidone in vitro.

(j) Cell viability assay assessing the cytotoxic effects of paliperidone on GSCs, DGCs, and NSCs.

(k) Dot blot analysis of m^1A levels in caRNAs isolated from cells treated with paliperidone for 48 h.

Figure 8

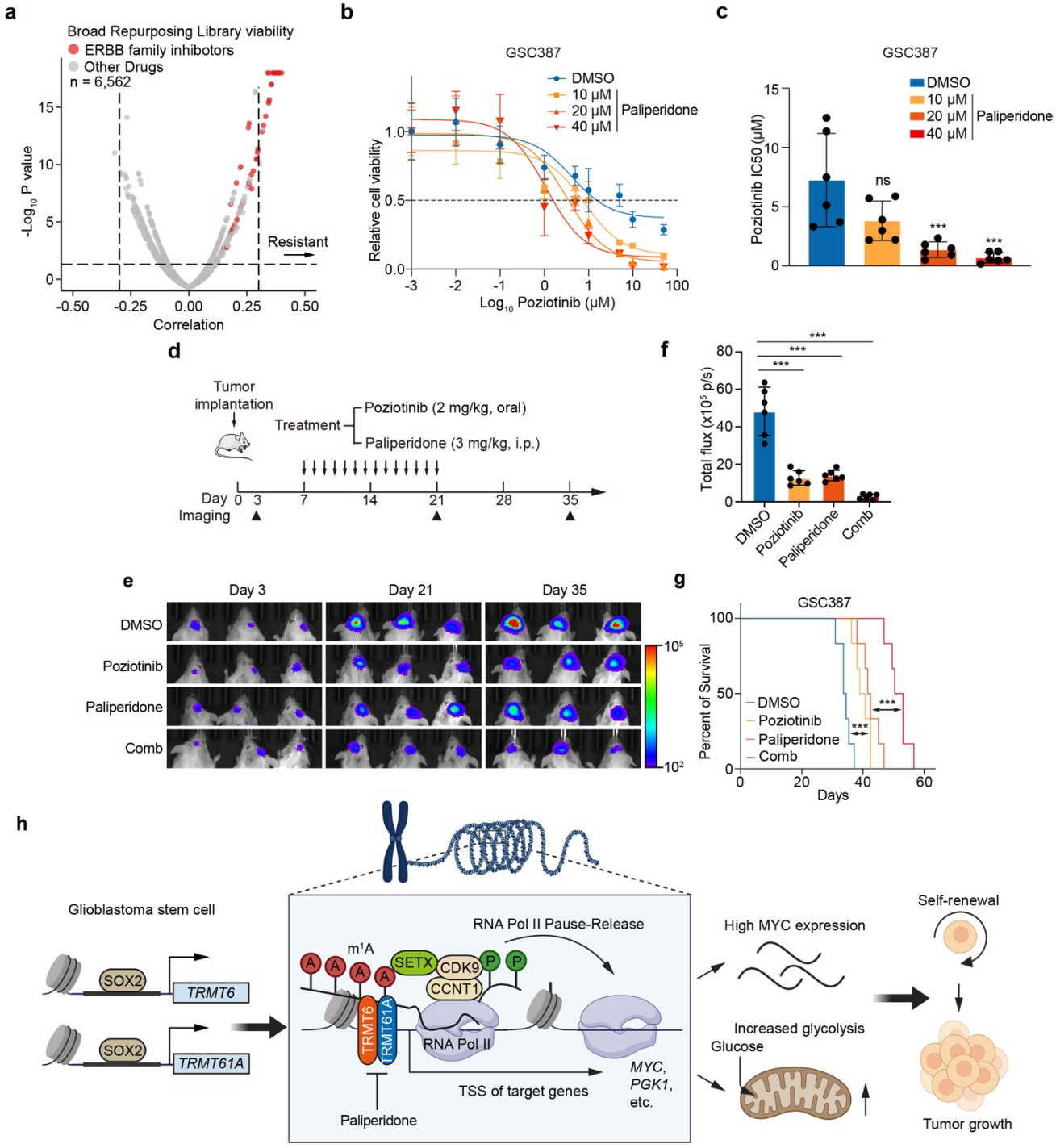
a
Broad Repurposing Library viability
ERBB family inhibotors
Other Drugs
n = 6,562
-Log10 P value
Correlation
Resistant
b
GSC387
DMSO
10 μM
20 μM
40 μM
Paliperidone
Relative cell viability
Log10 Poziotinib (μM)
c
GSC387
Poziotinib IC50 (μM)
ns
d
Tumor implantation
Treatment
Poziotinib (2 mg/kg, oral)
Paliperidone (3 mg/kg, i.p.)
Day
Imaging
e
Day 3
Day 21
Day 35
DMSO
Poziotinib
Paliperidone
Comb
f
Total flux (x10⁵ p/s)
g
GSC387
Percent of Survival
Days
h
Glioblastoma stem cell
SOX2
TRMT6
TRMT61A
m¹A
SETX
CDK9
CCNT1
RNA Pol II Pause-Release
RNA Pol II
TSS of target genes
MYC, PGK1, etc.
Paliperidone
High MYC expression
Increased glycolysis
Glucose
Self-renewal
Tumor growth

Fig. 8 Paliperidone sensitizes GSCs to ERBB inhibition.

(a) DepMap PRISM pharmacogenomic analysis showing the correlation between the core m^{1}A-regulated gene signature and drug response AUC values across the Broad Repurposing Library viability dataset. ERBB family inhibitors are highlighted in red. Positive correlation indicates higher m^{1}A gene signature expression and reduced drug sensitivity.

(b) Dose–response curves of GSC387 cells treated with increasing concentrations of poziotinib in combination with DMSO or the indicated concentrations of paliperidone.

(c) Quantification of poziotinib IC_{50} values in GSC387 cells treated with DMSO or increasing concentrations of paliperidone.

(d) Schematic of the in vivo treatment strategy. Mice bearing GSC387-luciferase xenografts were treated beginning 7 days after tumor implantation with poziotinib, paliperidone, or the combination for 2 weeks. Tumor burden was monitored by bioluminescence imaging at the indicated time points.

(e) Representative bioluminescence images of mice from each treatment group at days 3, 21, and 35 after tumor implantation.

(f) Quantification of tumor-associated bioluminescence signals at day 35 for each group.

(g) Kaplan–Meier survival curves of mice bearing GSC387 xenografts treated with DMSO, poziotinib, paliperidone, or the combination (n=6). *P* values were determined using the log-rank test. ***p < 0.001.

(h) Proposed model in which SOX2 upregulates TRMT6 and TRMT61A in GSCs, leading to caRNA m^{1}A deposition near target gene promoters. caRNA m^{1}A promotes SETX-associated RNA Pol II pause release and productive transcriptional elongation, thereby sustaining MYC expression, glycolytic programs, self-renewal, and tumor growth. Paliperidone binds TRMT61A and suppresses this caRNA m^{1}A-dependent transcriptional program. Data represent mean ± SD. *P* value was determined using one-way ANOVA with Bonferroni correction. ***p < 0.001.

Extended Data Figure 1

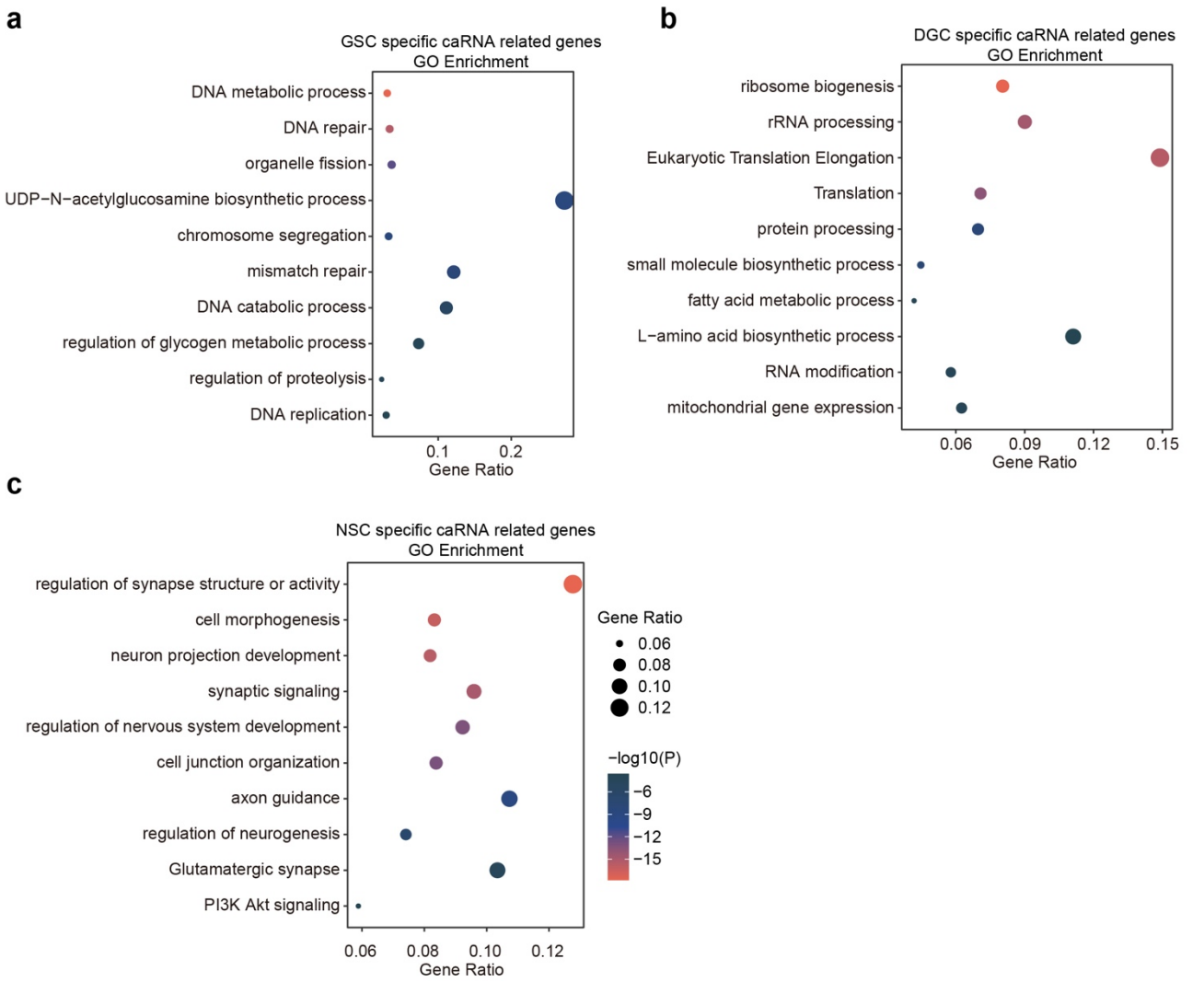

Extended data fig. 1 Gene Ontology analysis of genes with caRNAs.

(a-c) Gene ontology analysis was performed using genes associated with caRNAs in GSCs (A), DGCs (B), and NSCs (C).

Extended Data Figure 2

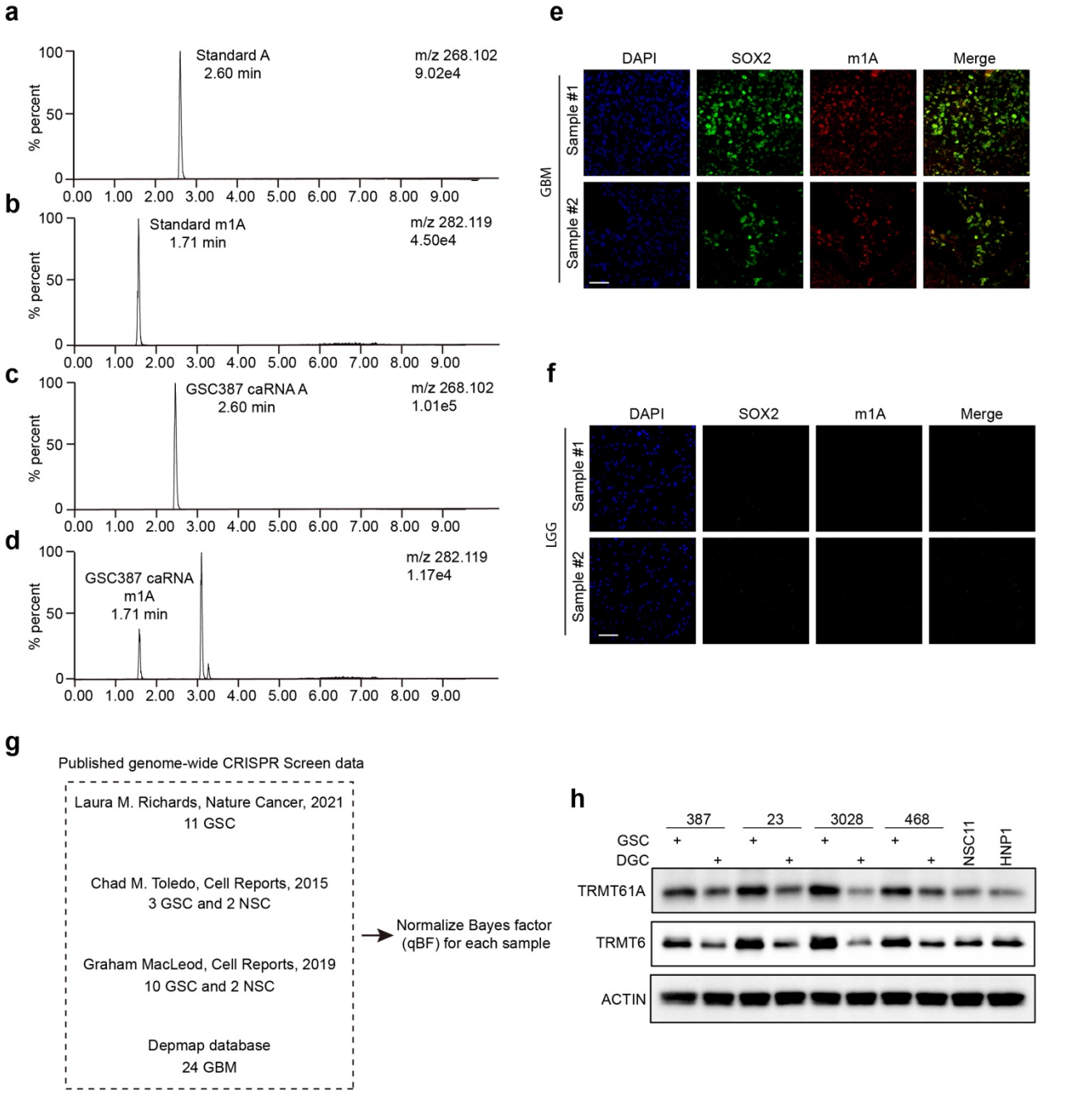

Extended data fig. 2. Quantification of m^1A abundance and identification of the TRMT6/61A complex in GSCs.

(a-d) Quantitative LC-MS/MS analysis of adenosine and m^1A peaks. Chromatograms display standards for adenosine (A) and m^1A (B) alongside nucleosides digested from caRNAs in GSC387 (C), and m^1A signals from GSC387 caRNAs (D). The x-axis represents retention time. The top-right inset shows the molecular weight and the maximum peak height.

(e and f) Immunofluorescence staining of m^1A and SOX2 in clinical specimens derived from GBM (E) and low-grade glioma (F). Scale bars represent 50 μm.

(g) Summary of genome-wide CRISPR screening datasets used to identify essential regulators of RNA modification in GSCs.

(h) Immunoblot analysis showing the protein levels of TRMT6 and TRMT61A across a panel of GSC, DGC, and NSC lines. Actin served as the loading control.

Extended Data Figure 3

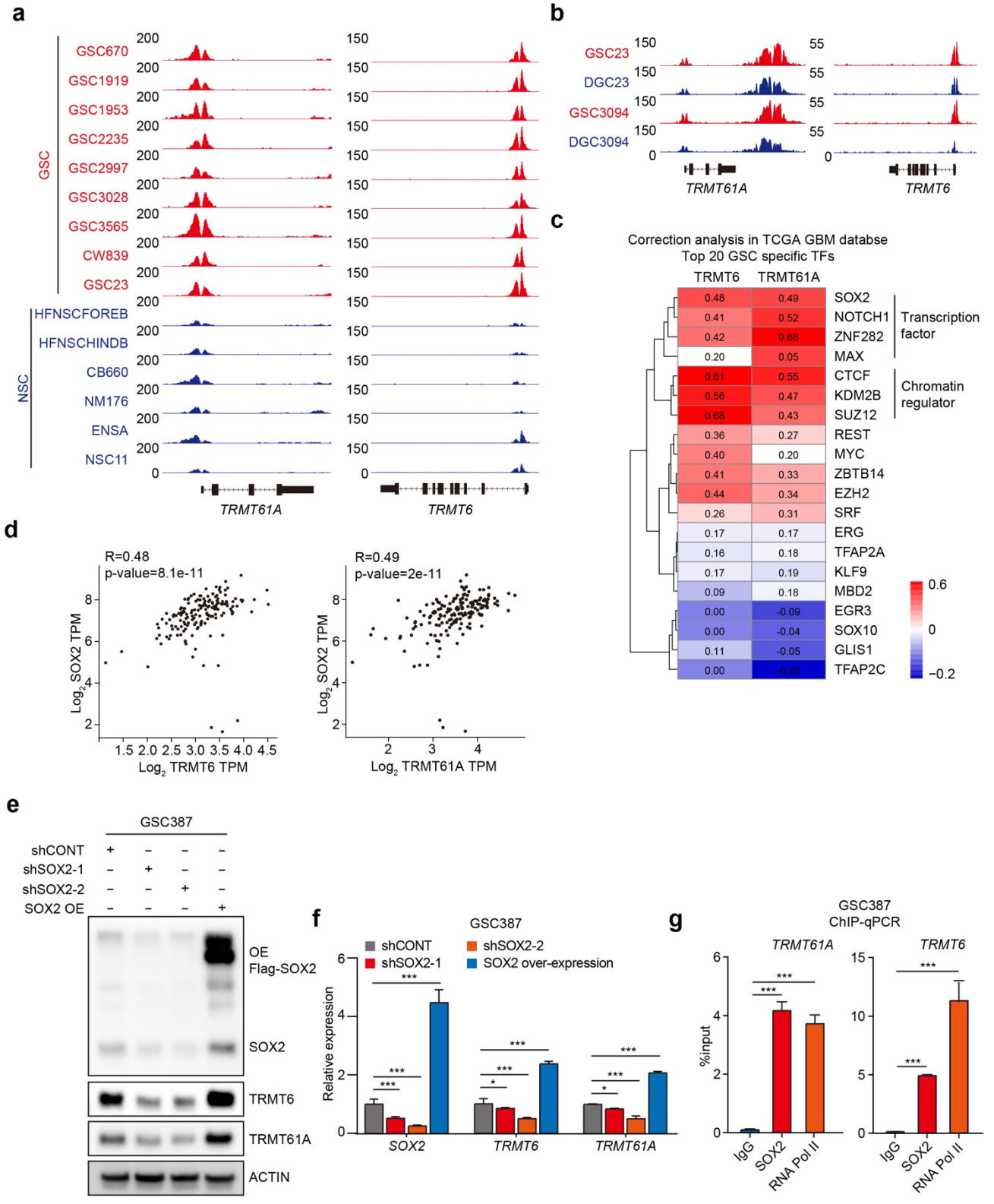

Extended data fig. 3. SOX2 acts as an upstream transcriptional activator of TRMT6 and TRMT61A.

(a and b) Genome browser views of H3K27ac ChIP sequencing signals at TRMT6 and TRMT61A promoters in GSCs relative to NSCs (A) and DGCs (B).

(c) Correlation analysis between TRMT6 or TRMT61A and transcription factors specific to GSCs using TCGA dataset.

(d) Correlation analysis between SOX2 and both TRMT6 and TRMT61A using TCGA dataset.

(e) western blotting showing protein levels of SOX2, TRMT6, and TRMT61A following knockdown or overexpression of SOX2 in GSC387.

(f) qPCR analysis of TRMT6 and TRMT61A mRNA levels following knockdown or overexpression of SOX2. Data are presented as the mean ± SD. *P* values were determined using one-way analysis of variance (ANOVA) with Bonferroni correction. *$p < 0.05$, ***$p < 0.001$.

(g) ChIP-qPCR confirming direct binding of SOX2 to the promoter regions of TRMT6 and TRMT61A. IgG was used as a negative control and RNA Polymerase II was used as a positive control. Data are presented as the mean ± SD. *P* values were determined using one-way analysis of variance (ANOVA) with Bonferroni correction. ***$p < 0.001$.

Extended Data Figure 4

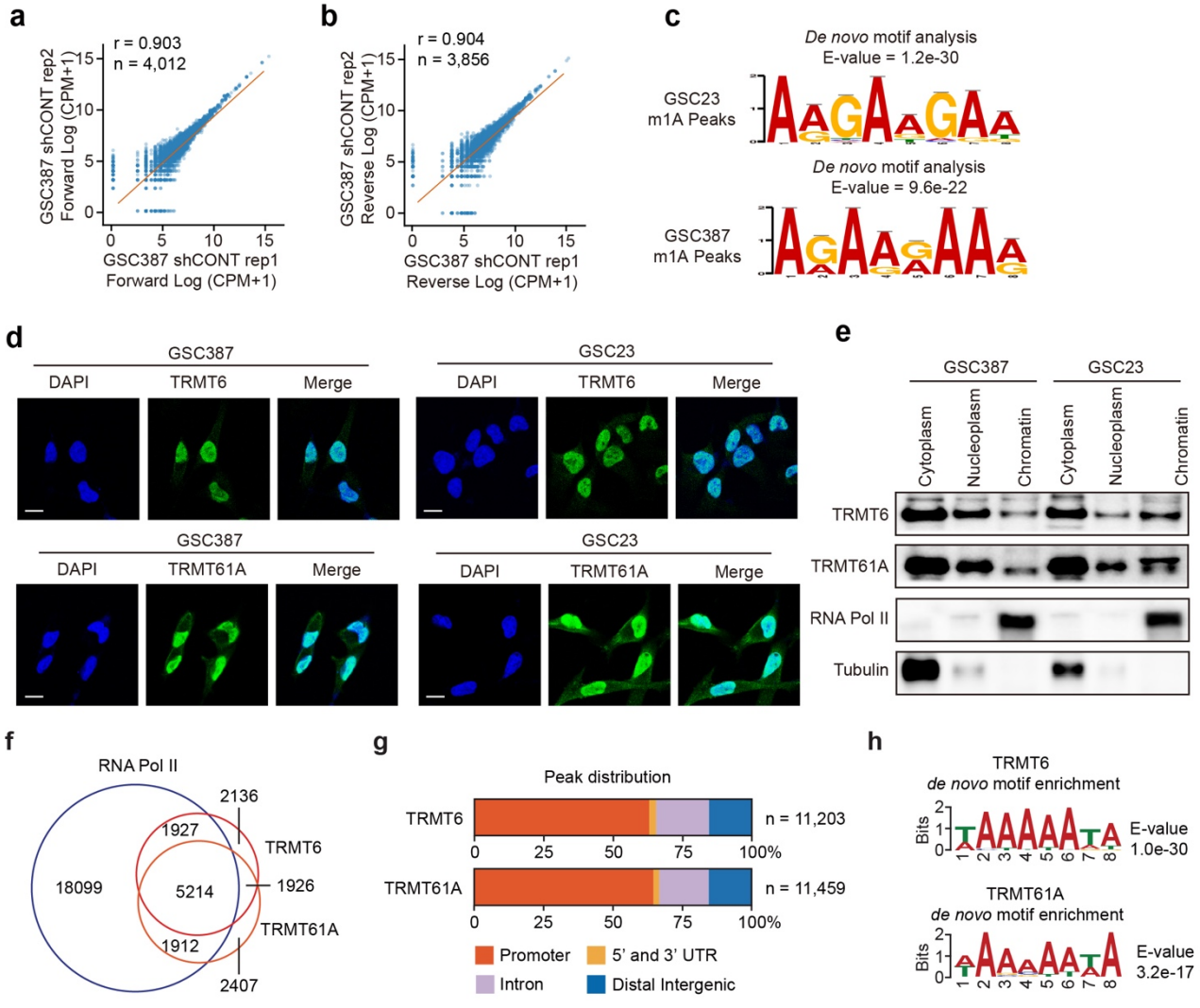

Extended data fig. 4. RIP-seq and TRMT6/61A ChIP-Seq analysis.

(a-b) Correlation analysis between two biologically independent GSC387 replicates, with each dot representing an individual peak quantified by counts per million (CPM).

(c) De novo motif analysis of the m^1A peak regions using the MEME suite revealing a preference for sequences rich in adenine.

(d) Representative immunofluorescence images of endogenous TRMT6 and TRMT61A in GSC387 and GSC23, showing predominant nuclear localization. Scale bars represent 10 μm.

(e) Western blot analysis of subcellular fractions, including the cytoplasm, nucleoplasm, and chromatin, to detect TRMT6 and TRMT61A. Tubulin and RNA Polymerase II served as markers for the cytoplasm and chromatin, respectively.

(f) Peak overlap analysis showing that the binding peaks of TRMT6 and TRMT61A coincided with RNA Polymerase II peaks.

(g) Genomic annotations illustrating the distribution of TRMT6 and TRMT61A binding peaks across gene-coding regions.

(h) De novo motif analysis of DNA sequences bound by the TRMT6 and TRMT61A complex, revealing enrichment for adenine-rich sequences.

Extended Data Figure 5

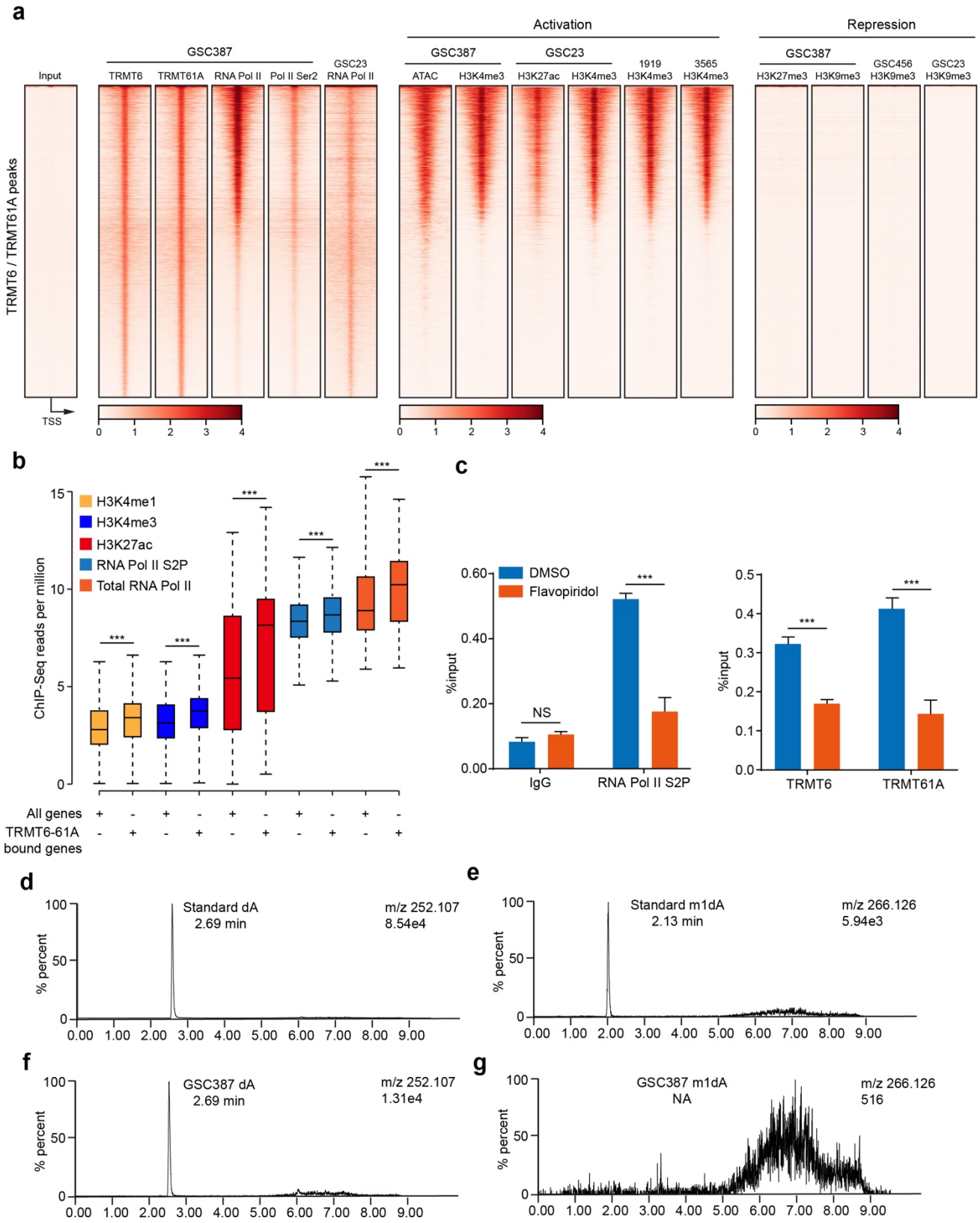

Extended data fig. 5. Genomic occupancy and relationship with transcription of TRMT6 and TRMT61A.

(a) Heatmap displaying the occupancy of RNA Polymerase II and markers of transcriptional activation and repression of the binding peaks of TRMT6 and TRMT61A.

(b) Box plot showing reads per million for H3K4me1, H3K4me3, H3K27ac, RNA Polymerase II, and Ser2P comparing target genes bound by TRMT6 and TRMT61A against non-target genes. *P* values were calculated using Wilcoxon test. ***p < 0.001.

(c) ChIP-qPCR showing reduced chromatin occupancy of TRMT6 and TRMT61A at the *MYC* promoter following treatment with the CDK9 inhibitor, flavopiridol (10 μM, 6 h). IgG served as a negative control and Ser2 phosphorylated RNA Polymerase II was used as a positive control. Data are presented as the mean ± SD. *P* values were determined using an unpaired t-test. ***p < 0.001.

(d-g) Liquid chromatography coupled with tandem mass spectrometry analysis of genomic DNA. Chromatograms display standards for deoxyadenosine (d) and N^1-methyldeoxyadenosine (e) along with nucleosides digested from GSC387 genomic DNA (f) and m^1dA signals from the same sample (g). The x-axis represents retention time. The top-right inset shows the molecular weight and the maximum peak height.

Extended Data Figure 6

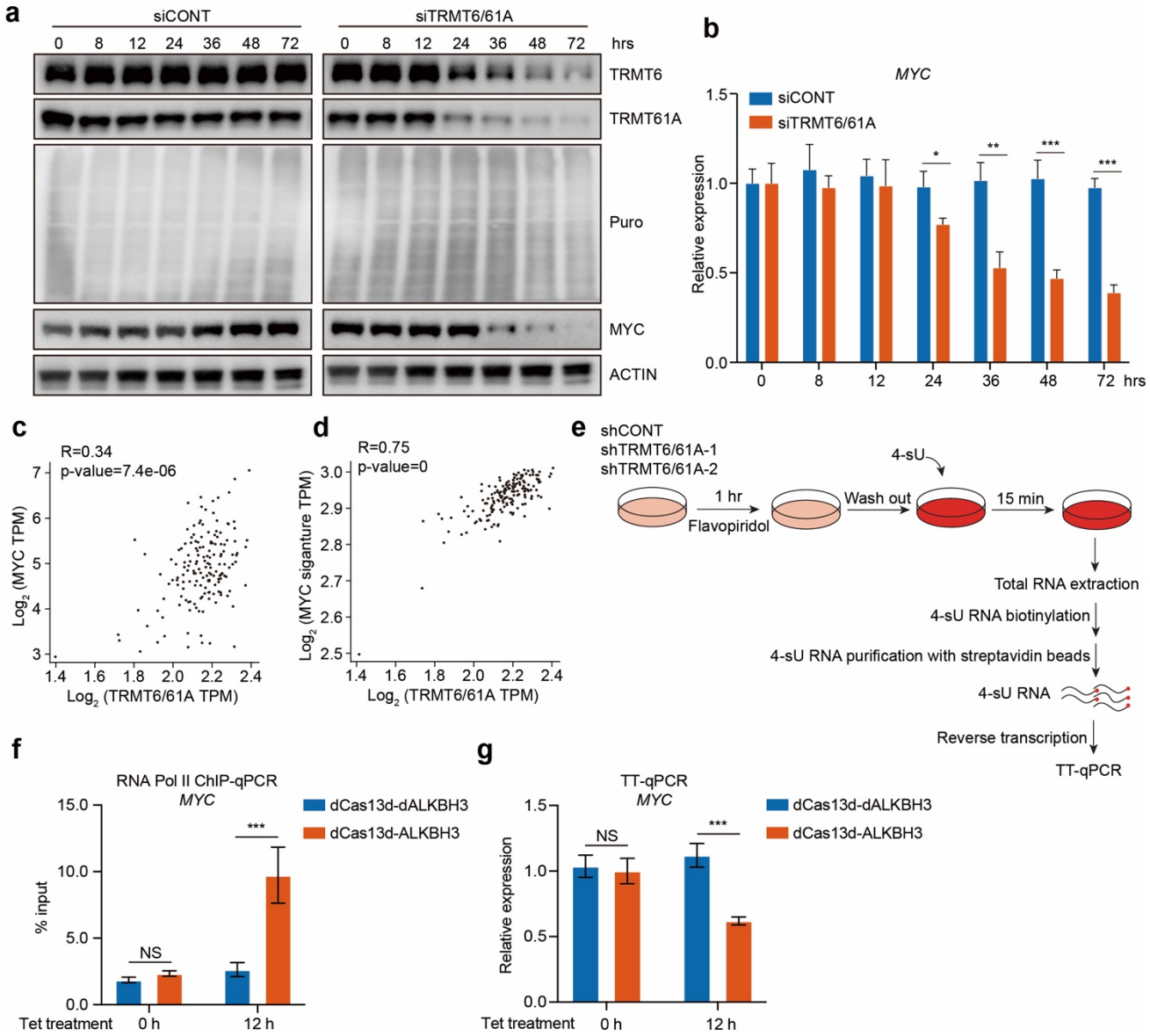

Extended data fig. 6. m^1A promotes transcriptional elongation.

(a and b) GSCs were transfected with siRNAs targeting TRMT6 and TRMT61A and labeled with 1 μM puromycin for 30 min at the indicated time points. Cells were then harvested for analysis of MYC protein (a) and mRNA (b) levels.

(c and d) Correlation analysis of TRMT6/61A expression with MYC expression (c) and the hallmark MYC target V1 signature (d) in the TCGA GBM dataset using GEPIA2.

(e) Schematic illustration of the transient transcriptome qPCR (TT-qPCR) strategy used to capture the nascent RNA. Cells in the control and knockdown groups were treated with CDK9 inhibitor to pause RNA Polymerase II. Following inhibitor washout, the cells were labeled with 500 μM 4sU for 15 min to mark nascent transcripts. RNA was extracted, biotinylated, and captured using streptavidin beads for qPCR analysis.

(f) ChIP qPCR analysis of RNA Polymerase II occupancy of the MYC promoter following induction with doxycycline for 12 h. Data are presented as the mean ± SD. *P* values were determined using an unpaired t-test. ***p < 0.001.

(g) Quantification of nascent MYC mRNA levels by transient transcriptome qPCR after treatment with doxycycline for 12 h. Data are presented as the mean ± SD. *P* values were determined using an unpaired t-test. ***p < 0.001.

Extended Data Figure 7

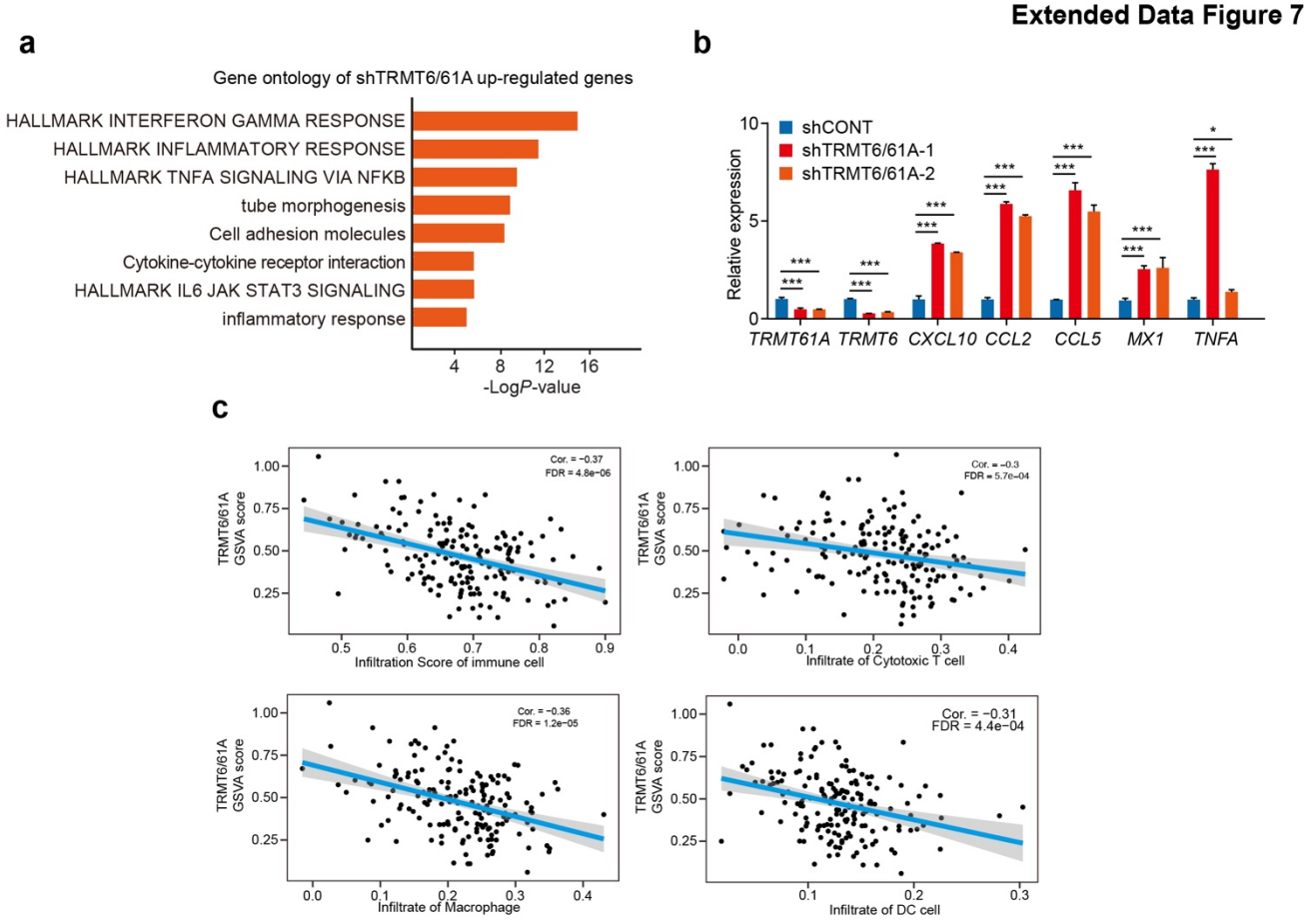

1133

Extended data fig. 7. TRMT6 and TRMT61A inhibition leads to activation of immune pathways.

(a) Gene Ontology analysis of the upregulated gene set showing the most enriched pathways.

(b) qPCR validation of representative genes involved in interferon gamma and inflammatory responses that were upregulated in cells depleted of TRMT6 and TRMT61A. Data are presented as the mean ± SD. Statistical significance was determined using one-way ANOVA. *$p < 0.05$, ***$p < 0.001$.

(c) Correlation analysis between the expression of TRMT6 and TRMT61A and the immune infiltration levels of cytotoxic CD8 + T cells, macrophages, and dendritic cells in TCGA samples using the GSCA tool (https://guolab.wchscu.cn/GSCA/#/).

Extended Data Figure 8

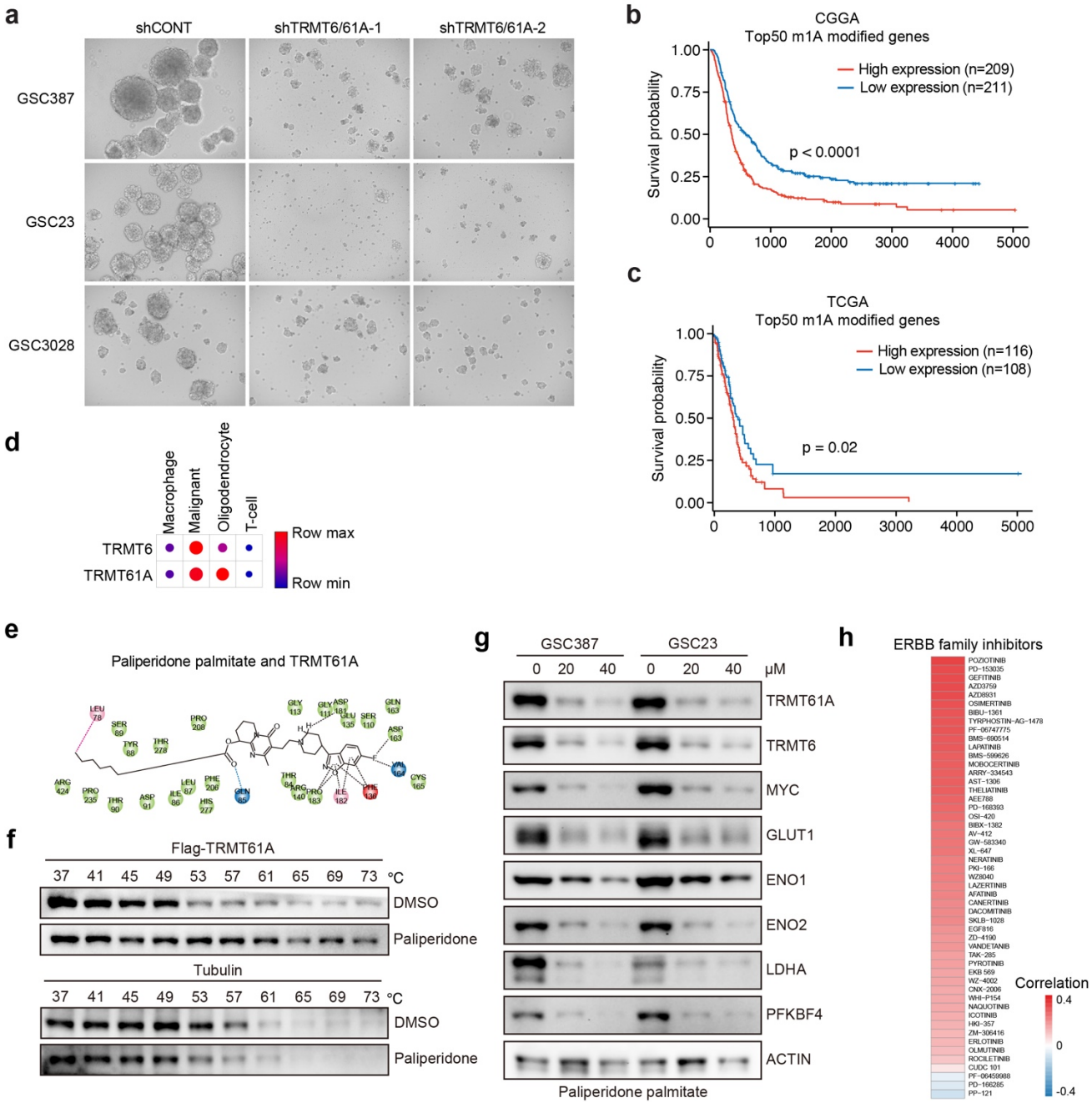

Extended data fig. 8. Paliperidone targets TRMT61A and combination with ERBB inhibition.

(a) Representative images of extreme limiting dilution assays in GSC387, GSC23, and GSC3028 cells following knockdown of TRMT6 and TRMT61A.

(b and c) Kaplan Meier analysis of patient survival in the CGGA (b) and TCGA (c) datasets stratified by the m^1A level of the top 50 genes. P values were calculated using the log-rank test.

(d) Single-cell RNA-seq analysis of TRMT6 and TRMT61A mRNA expression across different cell types in human GBM tissues (https://singlecell.broadinstitute.org/).

(e) Predicted binding mode of paliperidone palmitate within the TRMT61A binding pocket, based on molecular docking analysis. Key interacting residues are shown.

(f) Cellular thermal shift assay (CETSA) showing thermal stabilization of Flag-TRMT61A in cells treated with paliperidone compared to the DMSO control. Tubulin was used as a loading control.

(g) Western blot analysis of TRMT61A, TRMT6, MYC, and glycolysis-related proteins in GSC387 and GSC23 cells treated with paliperidone palmitate for 48 h. ACTIN was used as a loading control.

(h) Heatmap showing the correlation between the core m^1A-regulated gene signature and the drug response to ERBB family inhibitors in the DepMap PRISM pharmacogenomic dataset. Red indicates a positive correlation with the AUC, corresponding to reduced drug sensitivity, whereas blue indicates a negative correlation.

REFERENCES

1 Neftel, C. *et al.* An Integrative Model of Cellular States, Plasticity, and Genetics for Glioblastoma. *Cell* 178, 835-849 e821, (2019).

2 Lathia, J. D., Mack, S. C., Mulkearns-Hubert, E. E., Valentim, C. L. & Rich, J. N. Cancer stem cells in glioblastoma. *Genes Dev* 29, 1203-1217, (2015).

3 Mitchell, K., Troike, K., Silver, D. J. & Lathia, J. D. The evolution of the cancer stem cell state in glioblastoma: emerging insights into the next generation of functional interactions. *Neuro Oncol* 23, 199-213, (2021).

4 Singh, S. K. *et al.* Identification of human brain tumour initiating cells. *Nature* 432, 396-401, (2004).

5 Bao, S. *et al.* Glioma stem cells promote radioresistance by preferential activation of the DNA damage response. *Nature* 444, 756-760, (2006).

6 Bao, S. *et al.* Stem cell-like glioma cells promote tumor angiogenesis through vascular endothelial growth factor. *Cancer Res* 66, 7843-7848, (2006).

7 Mack, S. C. *et al.* Chromatin landscapes reveal developmentally encoded transcriptional states that define human glioblastoma. *J Exp Med* 216, 1071-1090, (2019).

8 Liau, B. B. *et al.* Adaptive Chromatin Remodeling Drives Glioblastoma Stem Cell Plasticity and Drug Tolerance. *Cell Stem Cell* 20, 233-246.e237, (2017).

9 Suvà, M. L. *et al.* Reconstructing and reprogramming the tumor-propagating potential of glioblastoma stem-like cells. *Cell* 157, 580-594, (2014).

10 Roundtree, I. A., Evans, M. E., Pan, T. & He, C. Dynamic RNA Modifications in Gene Expression Regulation. *Cell* 169, 1187-1200, (2017).

11 Delaunay, S., Helm, M. & Frye, M. RNA modifications in physiology and disease: towards clinical applications. *Nature Reviews Genetics* 25, 104-122, (2024).

12 Deng, X. *et al.* Epitranscriptomic control of cancer hallmarks: Functions, mechanisms, and therapeutics of RNA modifications. *Cancer Cell*, (2025).

13 Barbieri, I. & Kouzarides, T. Role of RNA modifications in cancer. *Nature Reviews Cancer* 20, 303-322, (2020).

14 Deng, X., Qing, Y., Horne, D., Huang, H. & Chen, J. The roles and implications of RNA m(6)A modification in cancer. *Nat Rev Clin Oncol* 20, 507-526, (2023).

15 Xiang, Y. *et al.* RNA m(6)A methylation regulates the ultraviolet-induced DNA damage response. *Nature* 543, 573-576, (2017).

16 Vu, L. P. *et al.* The N(6)-methyladenosine (m(6)A)-forming enzyme METTL3 controls myeloid differentiation of normal hematopoietic and leukemia cells. *Nat Med* 23, 1369-1376, (2017).

17 Zaccara, S., Ries, R. J. & Jaffrey, S. R. Reading, writing and erasing mRNA methylation. *Nat Rev Mol Cell Biol* 20, 608-624, (2019).

18 Meyer, K. D. *et al.* Comprehensive analysis of mRNA methylation reveals enrichment in 3' UTRs and near stop codons. *Cell* 149, 1635-1646, (2012).

19 Meyer, K. D. *et al.* 5' UTR m(6)A Promotes Cap-Independent Translation. *Cell* 163, 999-1010, (2015).

20 Cui, Q. *et al.* m(6)A RNA Methylation Regulates the Self-Renewal and Tumorigenesis of Glioblastoma Stem Cells. *Cell Rep* 18, 2622-2634, (2017).

21 Zhang, S. *et al.* m(6)A Demethylase ALKBH5 Maintains Tumorigenicity of Glioblastoma Stem-like Cells by Sustaining FOXM1 Expression and Cell Proliferation Program. *Cancer Cell* 31, 591-606.e596, (2017).

22 Yankova, E. *et al.* Small-molecule inhibition of METTL3 as a strategy against myeloid leukaemia. *Nature* 593, 597-601, (2021).

23 Wu, X. *et al.* NAT10-dependent N(4)-acetylcytidine reprograms R-loops and promotes cancer stem cell growth. *Cell Rep* 45, 117408, (2026).

24 Lin, P. *et al.* RBBP6 maintains glioblastoma stem cells through CPSF3-dependent alternative polyadenylation. *Cell Discov* 10, 32, (2024).
25 Masamha, C. P. *et al.* CFIm25 links alternative polyadenylation to glioblastoma tumour suppression. *Nature* 510, 412-416, (2014).
26 Jiang, L. *et al.* ADAR1-mediated RNA editing links ganglioside catabolism to glioblastoma stem cell maintenance. *J Clin Invest* 132, (2022).
27 Zhou, J. *et al.* RNA cytosine methyltransferase NSUN5 promotes protein synthesis and tumorigenic phenotypes in glioblastoma. *Mol Oncol* 17, 1763-1783, (2023).
28 Cui, Q. *et al.* Targeting PUS7 suppresses tRNA pseudouridylation and glioblastoma tumorigenesis. *Nat Cancer* 2, 932-949, (2021).
29 Li, X. & Fu, X. D. Chromatin-associated RNAs as facilitators of functional genomic interactions. *Nat Rev Genet* 20, 503-519, (2019).
30 Xu, W. *et al.* Dynamic control of chromatin-associated m(6)A methylation regulates nascent RNA synthesis. *Mol Cell* 82, 1156-1168 e1157, (2022).
31 Xu, W. *et al.* METTL3 regulates heterochromatin in mouse embryonic stem cells. *Nature* 591, 317-321, (2021).
32 Liu, J. *et al.* N (6)-methyladenosine of chromosome-associated regulatory RNA regulates chromatin state and transcription. *Science* 367, 580-586, (2020).
33 Zou, Z. *et al.* RNA m(5)C oxidation by TET2 regulates chromatin state and leukaemogenesis. *Nature* 634, 986-994, (2024).
34 Tao, E. W. *et al.* TRMT6-mediated tRNA m(1)A modification acts as a translational checkpoint of histone synthesis and facilitates colorectal cancer progression. *Nat Cancer*, (2025).
35 Liu, Y. *et al.* tRNA-m(1)A modification promotes T cell expansion via efficient MYC protein synthesis. *Nat Immunol* 23, 1433-1444, (2022).
36 Sun, Y. *et al.* m(1)A in CAG repeat RNA binds to TDP-43 and induces neurodegeneration. *Nature* 623, 580-587, (2023).
37 Sathyamoorthy, B. *et al.* Insights into Watson-Crick/Hoogsteen breathing dynamics and damage repair from the solution structure and dynamic ensemble of DNA duplexes containing m1A. *Nucleic Acids Res* 45, 5586-5601, (2017).
38 Barraud, P. *et al.* Crystal structure of Thermus thermophilus tRNA m1A58 methyltransferase and biophysical characterization of its interaction with tRNA. *J Mol Biol* 377, 535-550, (2008).
39 Dai, X., Wang, T., Gonzalez, G. & Wang, Y. Identification of YTH Domain-Containing Proteins as the Readers for N1-Methyladenosine in RNA. *Anal Chem* 90, 6380-6384, (2018).
40 Liu, F. *et al.* ALKBH1-Mediated tRNA Demethylation Regulates Translation. *Cell* 167, 816-828.e816, (2016).
41 Li, X. *et al.* Transcriptome-wide mapping reveals reversible and dynamic N1-methyladenosine methylome. *Nature Chemical Biology* 12, 311-316, (2016).
42 Safra, M. *et al.* The m1A landscape on cytosolic and mitochondrial mRNA at single-base resolution. *Nature* 551, 251-255, (2017).
43 Dominissini, D. *et al.* The dynamic N(1)-methyladenosine methylome in eukaryotic messenger RNA. *Nature* 530, 441-446, (2016).
44 Richards, L. M. *et al.* Gradient of Developmental and Injury Response transcriptional states defines functional vulnerabilities underpinning glioblastoma heterogeneity. *Nat Cancer* 2, 157-173, (2021).
45 Toledo, C. M. *et al.* Genome-wide CRISPR-Cas9 Screens Reveal Loss of Redundancy between PKMYT1 and WEE1 in Glioblastoma Stem-like Cells. *Cell Rep* 13, 2425-2439, (2015).
46 MacLeod, G. *et al.* Genome-Wide CRISPR-Cas9 Screens Expose Genetic Vulnerabilities and Mechanisms of

Temozolomide Sensitivity in Glioblastoma Stem Cells. *Cell Rep* 27, 971-986 e979, (2019).
47 Arafeh, R., Shibue, T., Dempster, J. M., Hahn, W. C. & Vazquez, F. The present and future of the Cancer Dependency Map. *Nat Rev Cancer* 25, 59-73, (2025).
48 Finer-Moore, J., Czudnochowski, N., O'Connell, J. D., 3rd, Wang, A. L. & Stroud, R. M. Crystal Structure of the Human tRNA m(1)A58 Methyltransferase-tRNA(3)(Lys) Complex: Refolding of Substrate tRNA Allows Access to the Methylation Target. *J Mol Biol* 427, 3862-3876, (2015).
49 Guelorget, A. *et al.* Insights into the hyperthermostability and unusual region-specificity of archaeal Pyrococcus abyssi tRNA m1A57/58 methyltransferase. *Nucleic Acids Res* 38, 6206-6218, (2010).
50 Takuma, H. *et al.* Substrate tRNA recognition mechanism of eubacterial tRNA (m1A58) methyltransferase (TrmI). *J Biol Chem* 290, 5912-5925, (2015).
51 Ozanick, S. G., Bujnicki, J. M., Sem, D. S. & Anderson, J. T. Conserved amino acids in each subunit of the heteroligomeric tRNA m1A58 Mtase from Saccharomyces cerevisiae contribute to tRNA binding. *Nucleic Acids Res* 35, 6808-6819, (2007).
52 Yuan, H. *et al.* Lysine catabolism reprograms tumour immunity through histone crotonylation. *Nature* 617, 818-826, (2023).
53 Hahn, A. *et al.* Misregulation of mitochondrial 6mA promotes the propagation of mutant mtDNA and causes aging in C. elegans. *Cell Metab* 36, 2528-2541 e2511, (2024).
54 Feng, X. *et al.* Sequencing of N(6)-methyl-deoxyadenosine at single-base resolution across the mammalian genome. *Mol Cell* 84, 596-610 e596, (2024).
55 Wu, T. P. *et al.* DNA methylation on N(6)-adenine in mammalian embryonic stem cells. *Nature* 532, 329-333, (2016).
56 Xie, Q. *et al.* N(6)-methyladenine DNA Modification in Glioblastoma. *Cell* 175, 1228-1243 e1220, (2018).
57 He, H. *et al.* Age-related noncanonical TRMT6-TRMT61A signaling impairs hematopoietic stem cells. *Nat Aging* 4, 213-230, (2024).
58 Xie, S. *et al.* Programmable RNA N(1) -Methyladenosine Demethylation by a Cas13d-Directed Demethylase. *Angew Chem Int Ed Engl* 60, 19592-19597, (2021).
59 Vervoort, S. J. *et al.* Targeting transcription cycles in cancer. *Nat Rev Cancer* 22, 5-24, (2022).
60 Jonkers, I. & Lis, J. T. Getting up to speed with transcription elongation by RNA polymerase II. *Nat Rev Mol Cell Biol* 16, 167-177, (2015).
61 Luo, Z., Lin, C. & Shilatifard, A. The super elongation complex (SEC) family in transcriptional control. *Nat Rev Mol Cell Biol* 13, 543-547, (2012).
62 Liang, K. *et al.* Targeting Processive Transcription Elongation via SEC Disruption for MYC-Induced Cancer Therapy. *Cell* 175, 766-779 e717, (2018).
63 Han, Z. *et al.* A role for human senataxin in contending with pausing and backtracking during transcript elongation. *Mol Cell* 85, 4166-4182.e4110, (2025).
64 Ippolitov, D. *et al.* The Brain-Penetrant Pan-ErbB Inhibitor Poziotinib Effectively Targets HER2+ Breast Cancer Brain Metastases. *Cancer Res* 85, 1514-1529, (2025).
65 Tang, J., Wang, X., Xiao, D., Liu, S. & Tao, Y. The chromatin-associated RNAs in gene regulation and cancer. *Mol Cancer* 22, 27, (2023).
66 Chen, P. B., Chen, H. V., Acharya, D., Rando, O. J. & Fazzio, T. G. R loops regulate promoter-proximal chromatin architecture and cellular differentiation. *Nat Struct Mol Biol* 22, 999-1007, (2015).
67 Ji, X. *et al.* SR proteins collaborate with 7SK and promoter-associated nascent RNA to release paused polymerase. *Cell* 153, 855-868, (2013).
68 Peterlin, B. M. & Price, D. H. Controlling the elongation phase of transcription with P-TEFb. *Mol Cell* 23, 297-

305, (2006).
69 Marshall, N. F., Peng, J., Xie, Z. & Price, D. H. Control of RNA polymerase II elongation potential by a novel carboxyl-terminal domain kinase. *J Biol Chem* 271, 27176-27183, (1996).
70 Zhu, Y. *et al.* Transcription elongation factor P-TEFb is required for HIV-1 tat transactivation in vitro. *Genes Dev* 11, 2622-2632, (1997).
71 Lin, C. *et al.* AFF4, a component of the ELL/P-TEFb elongation complex and a shared subunit of MLL chimeras, can link transcription elongation to leukemia. *Mol Cell* 37, 429-437, (2010).
72 Schulze-Gahmen, U. *et al.* The AFF4 scaffold binds human P-TEFb adjacent to HIV Tat. *Elife* 2, e00327, (2013).
73 Gu, J. *et al.* Crystal structure of HIV-1 Tat complexed with human P-TEFb and AFF4. *Cell Cycle* 13, 1788-1797, (2014).
74 Yang, H., Zhan, Y., Fenn, D., Chi, L. M. & Lam, S. L. Effect of 1-methyladenine on double-helical DNA structures. *FEBS Lett* 582, 1629-1633, (2008).
75 Wan, L., Lam, S. L., Lee, H. K. & Guo, P. Effects of Adenine Methylation on the Structure and Thermodynamic Stability of a DNA Minidumbbell. *Int J Mol Sci* 22, (2021).
76 Zhou, H. *et al.* m(1)A and m(1)G disrupt A-RNA structure through the intrinsic instability of Hoogsteen base pairs. *Nat Struct Mol Biol* 23, 803-810, (2016).
77 Lu, L., Yi, C., Jian, X., Zheng, G. & He, C. Structure determination of DNA methylation lesions N1-meA and N3-meC in duplex DNA using a cross-linked protein-DNA system. *Nucleic Acids Res* 38, 4415-4425, (2010).
78 Delaney, J. C. & Essigmann, J. M. Mutagenesis, genotoxicity, and repair of 1-methyladenine, 3-alkylcytosines, 1-methylguanine, and 3-methylthymine in alkB Escherichia coli. *Proc Natl Acad Sci U S A* 101, 14051-14056, (2004).
79 Amin, R. *et al.* NAT10 promotes cancer metastasis by modulating p300/CBP activity through chromatin-associated tRNA. *Mol Cell* 85, 4526-4544.e4518, (2025).
80 Wu, Y. *et al.* RNA m(1)A methylation regulates glycolysis of cancer cells through modulating ATP5D. *Proc Natl Acad Sci U S A* 119, e2119038119, (2022).
81 Moser, J. C. *et al.* A subset analysis of clinical activity and pharmacodynamic biomarkers in patients with sarcomas in the phase 1 dose-escalation study of STC-15, a METTL3 inhibitor. *Journal of Clinical Oncology* 44, 11548-11548, (2026).
82 Dolder, C., Nelson, M. & Deyo, Z. Paliperidone for schizophrenia. *Am J Health Syst Pharm* 65, 403-413, (2008).
83 Kim, D., Paggi, J. M., Park, C., Bennett, C. & Salzberg, S. L. Graph-based genome alignment and genotyping with HISAT2 and HISAT-genotype. *Nat Biotechnol* 37, 907-915, (2019).
84 Putri, G. H., Anders, S., Pyl, P. T., Pimanda, J. E. & Zanini, F. Analysing high-throughput sequencing data in Python with HTSeq 2.0. *Bioinformatics* 38, 2943-2945, (2022).
85 Love, M. I., Huber, W. & Anders, S. Moderated estimation of fold change and dispersion for RNA-seq data with DESeq2. *Genome Biol* 15, 550, (2014).
86 Zhou, Y. *et al.* Metascape provides a biologist-oriented resource for the analysis of systems-level datasets. *Nat Commun* 10, 1523, (2019).
87 Langmead, B., Trapnell, C., Pop, M. & Salzberg, S. L. Ultrafast and memory-efficient alignment of short DNA sequences to the human genome. *Genome Biol* 10, R25, (2009).
88 Ramírez, F. *et al.* deepTools2: a next generation web server for deep-sequencing data analysis. *Nucleic Acids Res* 44, W160-165, (2016).
89 Bailey, T. L., Johnson, J., Grant, C. E. & Noble, W. S. The MEME Suite. *Nucleic Acids Res* 43, W39-49, (2015).
90 Wang, Q. *et al.* Exploring Epigenomic Datasets by ChIPseeker. *Curr Protoc* 2, e585, (2022).
91 Robinson, J. T. *et al.* Integrative genomics viewer. *Nature Biotechnology* 29, 24-26, (2011).

92 Wang, K. *et al.* Genomic profiling of native R loops with a DNA-RNA hybrid recognition sensor. *Sci Adv* 7, (2021).
93 Chen, S., Zhou, Y., Chen, Y. & Gu, J. fastp: an ultra-fast all-in-one FASTQ preprocessor. *Bioinformatics* 34, i884-i890, (2018).
94 Zhang, Y. *et al.* Model-based analysis of ChIP-Seq (MACS). *Genome Biol* 9, R137, (2008).
95 Schwalb, B. *et al.* TT-seq maps the human transient transcriptome. *Science* 352, 1225-1228, (2016).
96 Dixit, D. *et al.* Glioblastoma stem cells reprogram chromatin in vivo to generate selective therapeutic dependencies on DPY30 and phosphodiesterases. *Sci Transl Med* 14, eabf3917, (2022).
97 Tang, Z., Kang, B., Li, C., Chen, T. & Zhang, Z. GEPIA2: an enhanced web server for large-scale expression profiling and interactive analysis. *Nucleic Acids Research* 47, W556-W560, (2019).
98 Bowman, R. L., Wang, Q., Carro, A., Verhaak, R. G. W. & Squatrito, M. GlioVis data portal for visualization and analysis of brain tumor expression datasets. *Neuro-Oncology* 19, 139-141, (2017).
99 Perez-Riverol, Y. *et al.* The PRIDE database at 20 years: 2025 update. *Nucleic Acids Res* 53, D543-d553, (2025).

Supplementary Files

This is a list of supplementary files associated with this preprint. Click to download.

- SupplementaryTables15.xlsx